

SIFTING FOR SAPPHIRES: SYSTEMATIC SELECTION OF TIDAL DISRUPTION EVENTS IN iPTF

T. HUNG¹, S. GEZARI^{1,2}, S.B. CENKO^{2,3}, S. VAN VELZEN^{2,4}, N. BLAGORODNOVA⁵, LIN YAN^{6,7}, S. R. KULKARNI⁵, R. LUNNAN⁸, T. KUPFER⁵, G. LELOUDAS⁹, A. K. H. KONG¹⁰, P. E. NUGENT^{11,12}, C. FREMLING⁵, RUSS R. LAHER⁷, F. J. MASCI⁷, Y. CAO^{13,14}, R. ROY⁸, AND T. PETRUSHEVSKA¹⁵

Draft version June 7, 2021

ABSTRACT

We present results from a systematic selection of tidal disruption events (TDEs) in a wide-area (4800 deg²), $g + R$ band, Intermediate Palomar Transient Factory (iPTF) experiment. Our selection targets typical optically-selected TDEs: bright (>60% flux increase) and blue transients residing in the center of red galaxies. Using photometric selection criteria to down-select from a total of 493 nuclear transients to a sample of 26 sources, we then use follow-up UV imaging with the Neil Gehrels Swift Telescope, ground-based optical spectroscopy, and light curve fitting to classify them as 14 Type Ia supernovae (SNe Ia), 9 highly variable active galactic nuclei (AGNs), 2 confirmed TDEs, and 1 potential core-collapse supernova. We find it possible to filter AGNs by employing a more stringent transient color cut ($g - r < -0.2$ mag); further, UV imaging is the best discriminator for filtering SNe, since SNe Ia can appear as blue, optically, as TDEs in their early phases. However, when UV-optical color is unavailable, higher precision astrometry can also effectively reduce SNe contamination in the optical. Our most stringent optical photometric selection criteria yields a 4.5:1 contamination rate, allowing for a manageable number of TDE candidates for complete spectroscopic follow-up and real-time classification in the ZTF era. We measure a TDE per galaxy rate of $1.7_{-1.3}^{+2.9} \times 10^{-4}$ gal⁻¹ yr⁻¹ (90% CL in Poisson statistics). This does not account for TDEs outside our selection criteria, thus may not reflect the total TDE population, which is yet to be fully mapped.

Keywords: accretion, accretion disks – black hole physics – galaxies: nuclei – ultraviolet: general

1. INTRODUCTION

A stellar tidal disruption event (TDE) refers to the phenomenon of a star being scattered into the Roche radius of a supermassive black hole. For a star approaching on a parabolic orbit, about half of the stellar debris remains bound to the black hole after the disruption. In the paradigm of TDEs, the circularized bound debris will

form an accretion disk and emit thermally (Rees 1988; Ulmer 1999) as it accretes onto the black hole. Alternatively, some studies have argued that the energy dissipated during the circularization process itself may be the main powering source of the emission in TDEs (Piran et al. 2015; Shiokawa et al. 2015; Dai et al. 2015; Bonnerot et al. 2017).

With the advent of a number of wide-field time domain surveys, about a dozen convincing optically bright TDEs have been discovered. Unlike the first few TDEs discovered in X-ray surveys (e.g. ROSAT) that have sparse light curves, the dense light curve sampling (once every few days) by ground-based optical surveys have enabled timely discoveries of these optical TDEs. The well-sampled optical light curves, together with the rapid follow-up observations across the electromagnetic spectrum, have provided rich data sets that allow us to study these TDEs in more detail. Although the selection criteria of these TDEs differ among surveys, most of them follow a power-law decline that is loosely consistent with $t^{-5/3}$ (Phinney 1989) in their light curves, while maintaining constant color over time. Most of these optically detected TDEs have a small spread in peak luminosity ($10^{43.4-44.4}$ erg s⁻¹) and blackbody temperature ($(2-4) \times 10^4$ K; Hung et al. 2017).

The first attempt of a systematic search of optically bright TDEs was made by van Velzen et al. (2011) using archival SDSS Stripe 82 imaging data, where they carefully examined the transients in the nuclei of galaxies (hereafter nuclear transients) and successfully recovered two TDE candidates. The search for TDEs usually excludes active host galaxies, because most AGNs exhibit variability and they outnumber TDEs by at least

¹ Department of Astronomy, University of Maryland, College Park, MD 20742, USA

² Joint Space-Science Institute, University of Maryland, College Park, MD 20742, USA

³ NASA Goddard Space Flight Center, Mail Code 661, Greenbelt, MD 20771, USA

⁴ Department of Physics, New York University, NY 10003, USA

⁵ Department of Astronomy, California Institute of Technology, Pasadena, CA 91125, USA

⁶ Caltech Optical Observatories, Cahill Center for Astronomy and Astrophysics, California Institute of Technology, Pasadena, CA 91125, USA

⁷ Infrared Processing and Analysis Center, California Institute of Technology, Pasadena, CA 91125, USA

⁸ The Oskar Klein Centre & Department of Astronomy, Stockholm University, AlbaNova, SE-106 91 Stockholm, Sweden

⁹ Dark Cosmology Centre, Niels Bohr Institute, University of Copenhagen, Juliane Maries vej 30, 2100 Copenhagen, Denmark

¹⁰ Institute of Astronomy, National Tsing Hua University, No. 101, Section 2, Kuang-Fu Road, Hsinchu, 30013, Taiwan

¹¹ Department of Astronomy, University of California, Berkeley, CA 94720-3411, USA

¹² Lawrence Berkeley National Laboratory, 1 Cyclotron Road, MS 50B-4206, Berkeley, CA 94720, USA

¹³ Department of Astronomy, University of Washington, Box 351580, U.W., Seattle, WA 98195-1580, USA

¹⁴ eScience Institute, University of Washington, Box 351570, U.W., Seattle, WA 98195-1580, USA

¹⁵ Oskar Klein Centre, Department of Physics, Stockholm University, SE 106 91 Stockholm, Sweden

two orders of magnitude. Follow-up on these sources is cost inefficient, since a detailed spectroscopic study would be required to differentiate between AGN variability and TDE signatures. Nevertheless, there is no mechanism prohibiting stars from being disrupted by active black holes. In fact, two events, CSS100217 (Drake et al. 2011) and the recently reported PS16dtm (Blanchard et al. 2017), have been claimed as TDEs occurring in narrow-line Seyfert 1 galaxies. Their properties, however, can be somewhat different from the TDEs observed in quiescent galaxies. For example, the light curve of PS16dtm exhibits a plateau instead of a monotonical decline following $t^{-5/3}$, even though its blackbody temperature remained constant at $T_{bb} \approx 1.7 \times 10^4$ K. The broad H α component (≈ 4000 km s $^{-1}$) in both CSS100217 and PS16dtm are considerably narrower than TDEs in inactive galaxies (10^4 km s $^{-1}$; Hung et al. 2017) and they exclusively exhibit strong Fe II emission complexes. In addition, both events were radiating near Eddington luminosity, which may suggest they are accreting more efficiently than TDEs in inactive galaxies (Blanchard et al. 2017).

Finding TDEs can also be complicated by the detection of transients in galaxy nuclei. Nuclear transient events suffer from stronger systematic and statistical errors when subtracted from the core of a galaxy. This poses a problem because large surveys like the intermediate Palomar Transient Factory (iPTF) rely on machine learning algorithms to remove image subtraction artifacts. Therefore, nuclear transients are more easily missed in this process of machine identification. Using the `realbogus` pipeline employed by iPTF as an example, the completeness drops from 1 to 0.5 when the flux contrast, defined as the ratio between the transient and the underlying host galaxy surface brightness, decreases from >10 times to 0.6 times (Frohmaier et al. 2017).

While the majority of the optically discovered TDEs reside in red early-type galaxies (see color definition in § 3.3), they seem to appear disproportionately more in a rare subset — quiescent Balmer-strong (E+A) galaxies — whose star formation history indicates they are in a post-starburst stage (Arcavi et al. 2014; French et al. 2016; Stone & van Velzen 2016). On a different study that employs a control group from SDSS, Law-Smith et al. (2017) found that TDE host galaxies have a higher nuclear stellar density that is not owing to a recent major merger. Although the rare E+A galaxies are reported to be over-represented by at least 35 times in the current TDE sample (French et al. 2016; Graur et al. 2017), it is not known whether TDEs preferentially occur in E+A host galaxies, or they occur more frequently in centrally overdense galaxies.

The ever-growing number of TDEs discovered in optical surveys have gradually alleviated the tension between the observed and the predicted TDE rates, where the observed rate is typically an order of magnitude lower than the theoretical value predicted from two-body relaxation of stars in realistic galaxies ($\gtrsim 10^{-4}$ gal $^{-1}$ yr $^{-1}$; Magorrian & Tremaine 1999; Wang & Merritt 2004; Stone & Metzger 2016). It is generally accepted that the lower observational TDE rate can be attributed to the fact that only the brighter TDEs in a steep TDE luminosity function are followed-up in flux-limited surveys (van Velzen

2017). The fact that the luminosities of most optical TDEs seem to be drawn from a distribution with a small spread (Hung et al. 2017) is also consistent with this scenario as long as the TDE luminosity is not a narrow step function. Since it is almost impossible to obtain a spectroscopically complete sample for most of the photometric surveys except for the All-Sky Automated Survey for Supernova (ASASSN has a flux limit of $r \sim 17$ mag; Shappee et al. 2014), at least some parts of this bias is introduced by human decisions on whether to trigger spectroscopic classification for a certain object. Therefore, a systematic strategy for selecting TDE candidates in real time for follow-up observations is critical for measuring TDE rates robustly.

Future surveys such as the Zwicky Transient Facility (ZTF) in 2018 and the Large Synoptic Survey Telescope (LSST) in the early 2020s are expected to boost the number of transients including TDEs by orders of magnitude. Maximizing the efficiency of follow-up resources will be even more challenging. In 2016, iPTF conducted its first experiment with simultaneous color observations. With a Cycle 12 *Swift* Key Project (PI Gezari) and observing time on several optical spectrographs, we were able to perform a systematic follow-up of the TDE candidates that satisfy the selection of our nuclear transient pipeline. Two TDEs, iPTF16axa ($z=0.108$) and iPTF16fnl ($z=0.016$), were discovered during this 4-month experiment. In particular, iPTF16fnl is the faintest and fastest TDE discovered yet with a decay rate of ~ 0.08 mag day $^{-1}$ (Blagorodnova et al. 2017a).

In this paper, we report the performance of our pipeline, which is optimized for TDEs by searching for blue ($g_{\text{PTF}} - R_{\text{PTF}} < 0$ mag) nuclear flares within inactive red host galaxies, and derive the TDE rate in iPTF. We first describe the design of the $g_{\text{PTF}} + R_{\text{PTF}}$ survey in § 2 and the selection of the nuclear candidates for *Swift* and spectroscopic follow-up in § 3. The photometric and spectroscopic observations are detailed in § 4. The classification of the final sample along with the results from *Swift* are presented in § 5. We discuss the performance of our pipeline and calculate the TDE rate in iPTF in § 6. We conclude by outlining the prospects of TDE discoveries with ZTF in § 6.

2. ROLLING $g+R$ SURVEY DESIGN

iPTF conducted a rolling $g + R$ experiment from UT 2016 May 28 to 2016 Dec 7, observing a total of 81 nights. The Palomar 48-inch (P48) telescope uses SDSS- g' and Mould- R filters (hereafter g_{PTF} and R_{PTF}) to carry out the survey. The experiment was suspended between 2016 Jun 16 and 2016 Aug 20 when the telescope time was entirely dedicated to the H α survey and the Galactic plane survey.

The experiment took place in two stages. In the later period from 2016 Aug 20 to Nov 10, it was strictly controlled using a rolling strategy that was implemented as follows. We divided the 270 fields in total into three groups of 90 fields. At any given time, one of the groups was observed using a 1-day cadence, while the remaining 180 fields were observed using a 3-day cadence (i.e. 60 each night). As such, the total number of fields observed each night was 150. The 1-day cadence group was rotated so that every field would cycle between 1-day and 3-day cadences. This rotation took place regularly every

lunation. Missed nights due to weather would become gaps in the light curve. To obtain the color, each field was observed with one g_{PTF} and one R_{PTF} filter typically separated by ~ 0.5 hr. This experiment was called the *Color Me Intrigued* experiment when it was proposed (see Miller et al. 2017, for more details).

In the earlier stage from 2016 May 28 to Jun 16, fewer fields (58 fields on average) were targeted in a night. Each field was observed three times in g_{PTF} and R_{PTF} filters per night with two observations in the same filter. All of the targeted fields were scheduled to have a 4-day cadence. This change in cadence from the latter rolling cadence strategy should have little impact on the outcome of our TDE search, since tidal disruption flares can last for months. Both TDEs iPTF16axa and iPTF16fnl were discovered in the 3-d cadence fields.

We present the sky coverage of the $g + R$ experiment in Fig. 1, with color bars indicating the number of exposures. The fields were selected to be overhead and have low airmass at the Palomar observatory during the observing period. We show the number of fields observed per night throughout the operation in the left panel of Fig. 2. Given the 7.26 deg^2 field of view of the telescope, this corresponds to an average areal coverage of 771 deg^2 per night. The right panel of Fig. 2 shows the distribution of the longest baseline in each field excluding the summer gap. In Fig. 3, the cadence distribution of the experiment is split by stages and by filters. In the early stage shown in the upper panel of Fig. 3, most of the targeted fields were observed twice in g_{PTF} band per night and have a 4-day cadence. The later stage shown in the lower panel peaks at 1, 3, 6 days as intended by the experiment strategy. In summary, The experiment monitored 660 unique fields, which corresponds to a total of 4792 deg^2 of the sky.

3. SELECTION OF CANDIDATES

During the $g_{\text{PTF}}+R_{\text{PTF}}$ experiment, the survey data was processed by the real-time image subtraction pipelines at the Infrared Processing and Analysis Center (IPAC) (Masci et al. 2017) and the National Energy Research Scientific Computing Center (NERSC) (Cao et al. 2016). We rely on machine learning classification — the probability based real-bogus (RB) score — to determine the likelihood of the detection being a real astrophysical transient, as opposed to a false detection caused by image subtraction artifacts (Masci et al. 2017). Sources that had a $S/N > 5$, a high RB score (> 0.6), and at least 2 co-spatial detections within one night that were not cataloged as a variable star or a quasar, were visually inspected by a human. Since bad subtractions normally have an irregular PSF, they can be readily recognized by eye. This process, called scanning, took place on a daily basis. Only sources approved by the scanners were saved to the database for further study.

We show the stacked histogram of the number of transients saved during this experiment in Fig. 4, where the nuclear and non-nuclear transients are shown in red and blue, respectively. A total of 1464 transients were saved in this period, averaging 18 transients per night.

In transient surveys, the rate of SNe Ia ($2.7 \times 10^{-5} \text{ yr}^{-1} \text{ Mpc}^{-3}$; Dilday et al. 2010) is on the order of 100 times higher than TDEs. Type 1 AGNs, which are known to be variable in the optical on timescales up to sev-

eral years (Sesar et al. 2007), have a space density of $\approx 7 \times 10^{-6} \text{ Mpc}^{-3}$ (Hao et al. 2005) that also outnumber TDEs by roughly two orders of magnitude. These two types of events are the main interlopers in the process of selecting TDE candidates. Because of their disproportionately higher occurrences, our selection criteria are focused on removing these interlopers, which we describe as follows.

The filtering has 7 steps (Fig. 5). We first select sources that are astrometrically aligned with the center of a morphologically extended host galaxy. We make a further cut based on host galaxy color, selecting only nuclear transients in red host galaxies. We then remove sources that are known AGN by cross-matching with external catalogs or checking for flaring history in the historical PTF and iPTF database since 2009. We exclude sources with weak variability by applying a magnitude cut. Lastly, we remove red transient events and sources that are too dim for spectroscopic follow up. The composition of each intermediate sample is listed in Table 1. The first column contains the description of each filtering procedure, which is detailed in the following sections.

3.1. Selection of Nuclear Transients (Step 1)

Tidal disruption of a star around a black hole occurs when the orbit of the star crosses the tidal disruption radius (R_T). For a non-spinning black hole, R_T is defined as

$$R_T = R_* \left(\frac{M_{\text{BH}}}{M_*} \right)^{1/3} = 0.47 \text{ AU} \left(\frac{R_*}{R_\odot} \right) \left(\frac{M_{\text{BH}}}{10^6 M_*} \right)^{1/3}, \quad (1)$$

where M_{BH} is the black hole mass, R_* and M_* are the radius and mass of the disrupted star, respectively. Since a TDE happens near the black hole, we limit our search to transients that reside in the center of a host galaxy. This tidal disruption radius corresponds to an angular separation on the nano-arcsecond scale at $z=0.1$ that cannot be resolved by any instrument.

We define a transient as nuclear if the separation of the transient and the centroid of the galaxy is less than $0.8''$. This radial cut was empirically determined to include 80% of the PTF transients in the database associated with known AGNs (Fig. 6). This offset distance is measured relative to the coordinates of the host centroid as output by SExtractor (Cao et al. 2016). While the mean position of the offset (relative right ascension $\Delta\alpha$ and declination $\Delta\delta$) over all detections should be zero, the offset distance between the transient and the host $x \approx \sqrt{\Delta\alpha^2 + \Delta\delta^2}$, should be non-zero (Fig. 6). The offset distance distribution can provide clues to the distribution of $\Delta\alpha$ and $\Delta\delta$. For example, if both $\Delta\alpha$ and $\Delta\delta$ are independent and normally distributed with the same variance and zero means, the offset distances can be characterized by a Rayleigh distribution that has the following form.

$$f(x; \sigma) = \frac{x}{\sigma^2} e^{-x^2/2\sigma^2}, \quad (2)$$

where x is the offset distance and σ is the standard deviation of the $\Delta\alpha$ and $\Delta\delta$ distributions. The mode ($0.4''$ in Fig. 6) of a Rayleigh distribution is equal to 1σ .

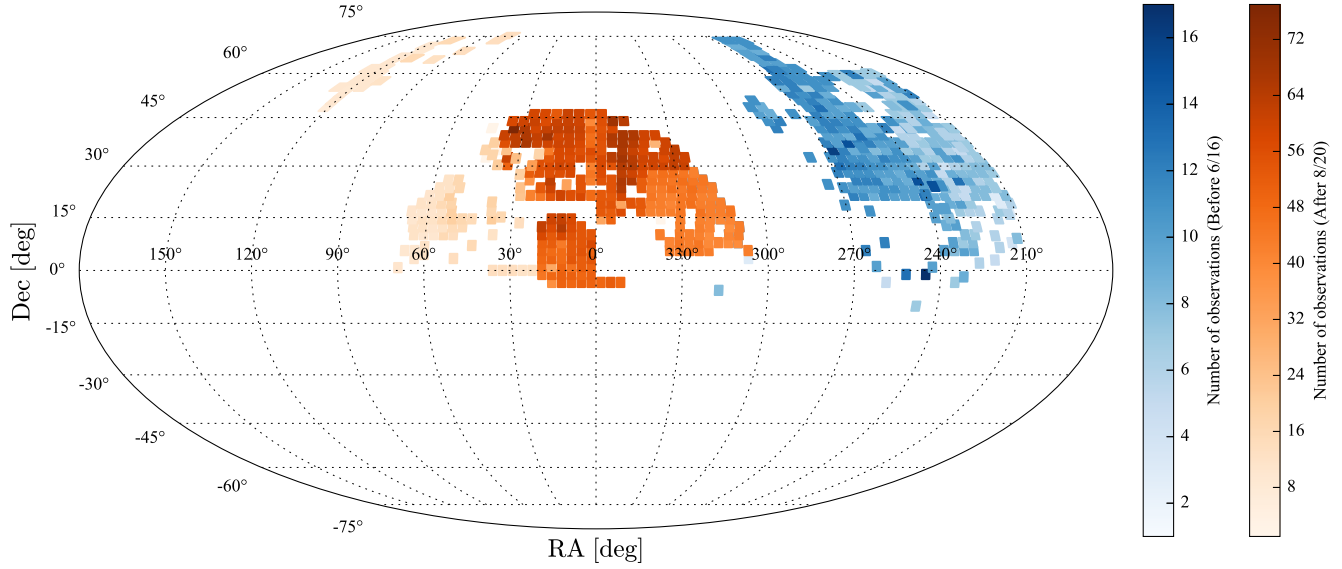


Figure 1. Sky coverage of the iPTF color experiment in Equatorial coordinates. The plot is broken down by the stage of the survey (before and after the summer hiatus). Each tile represents a unique pointing, and the color intensity reflects the number of observations in that field. Around 77% of the fields were also observed by SDSS.

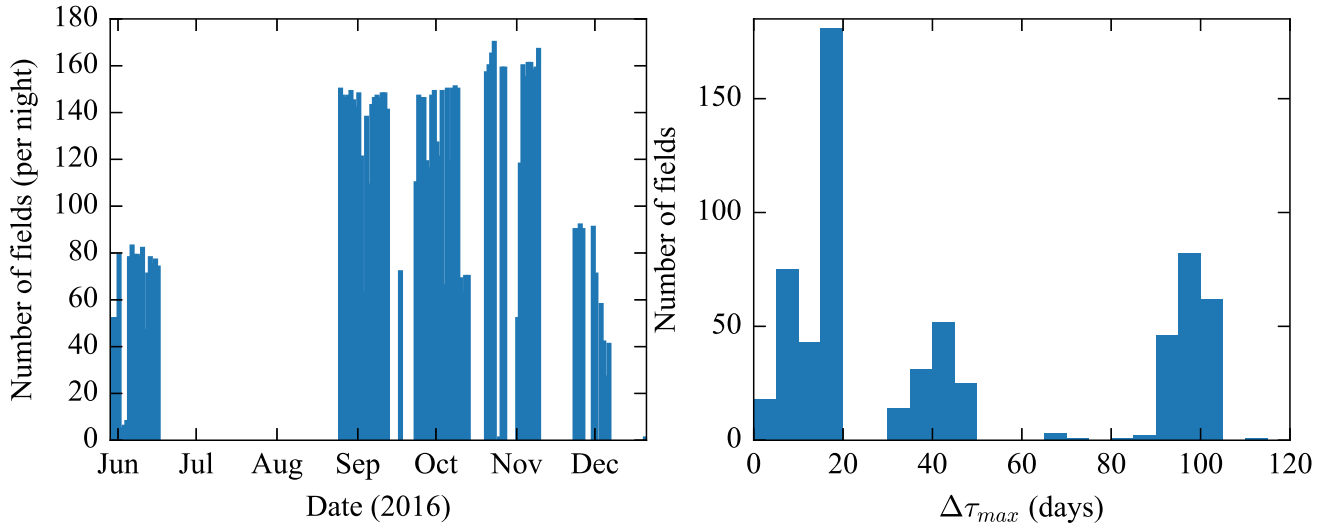


Figure 2. Left: number of unique fields observed per night during the $g_{\text{PTF}}+R_{\text{PTF}}$ survey. Fewer fields were observed before Aug 2016 because each field was observed three times (usually 2 in g_{PTF} and 1 R_{PTF}) per night instead of two. Right: distribution of the longest baseline of each field in the $g_{\text{PTF}}+R_{\text{PTF}}$ experiment.

Table 1
Sample composition after each filtering step

Selection	all	Host color blue	red	Known AGN	Historical Detection	$ \Delta m_{\text{var}} $ ≥ 0.5	≤ 0.5	$g_{\text{PTF}}-R_{\text{PTF}}$ ≤ 0	≥ 0	Peak mag ≤ 20	≥ 20
Nuclear	493	216	267	37	94	249	235	200	203	285	206
Extended host	375	150	225	31	62	189	186	158	157	221	154
Red host	225	...	225	12	37	81	144	78	105	136	89
Not known AGN	200	...	200	...	37	78	122	72	95	119	81
No variability history	163	...	163	69	94	62	73	90	73
$ \Delta m_{\text{var}} > 0.5$	69	...	69	69	...	33	30	46	23
Blue flare	33	...	33	33	...	33	...	26	7

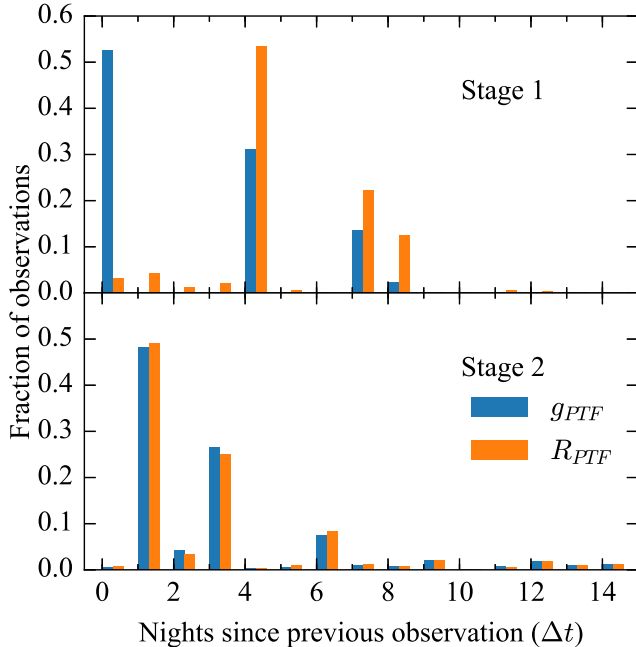


Figure 3. Cadence of the $g_{PTF} + R_{PTF}$ experiment in two stages. Plots show the fraction of Δt between any two adjacent epochs for all the unique fields observed during this period in g_{PTF} (blue) and R_{PTF} (orange) bands. The left bin edges of g_{PTF} band are aligned with the tick marks, with R_{PTF} offset to the right for clarity. Intra-night observations ($\Delta t=0$) are dominated by the observations made before August (upper panel), where two observations in the same filter were used to reject moving objects. The designed cadence of the later stage (bottom panel) is a rotating Δt of 1 and 3 days. The cadence for the later stage also clusters around 6 days due to weather loss.

Cross-matching to AGNs is intended to help us quantify the tolerance for scatter in offset distance for nuclear transients. We expect some of these matched transients to be caused by unidentified supernovae instead of nuclear activity. In fact, the tail of the offset distance distribution should be mostly contributed by these supernovae that went off near AGNs.

For each object, we calculate the median of the separation of all detections available at the time a transient was saved and apply the separation cut to remove 971 transients that are non-nuclear. On average, P48 detected 6 new nuclear transients and 12 non-nuclear transients per night for an average nightly coverage of 771 deg^2 . This corresponds to a surface density of 7.8×10^{-3} per deg^2 for nuclear transients on the sky.

3.2. Selection of Extended Hosts (Step 2)

We remove transients with unresolved hosts that are classified as a star or a quasar. We searched for host galaxies within a $3''$ radius of a transient using SDSS DR12 and PS1 DR1 catalogs. The SDSS star-galaxy separator comes with the `frames` pipeline and the results are stored in `type` under the `PhotoObjA11` table. In cases where a source is outside the imaging coverage of SDSS, we use measurements from PS1 3π Survey, which is available in DR1, to remove point-like sources. We define a point source as having $r_{\text{MeanPSFMag}} - r_{\text{MeanKronMag}} < 0$. This definition can segregate stars and galaxies with a 99% accuracy for galaxies brighter than 20 mag in the r band (Tachibana et al. in prep).

3.3. Selection of Red Galaxy Hosts (Step 3)

The major sources of contamination in the nuclear transient sample are SNe that fall inside the nuclear circle of a host galaxy and variable AGNs. While previously discovered TDEs seem to be found toward early-type galaxies, it has been well-established that core-collapse supernovae (CCSNe) are preferentially hosted by "blue" starforming galaxies (e.g. Kelly & Kirshner 2012). Therefore, we select only nuclear events hosted by red galaxies with empirically defined boundaries of $u - g > 1.0$ mag and $g - r > 0.5$ mag. This definition has worked well for previously discovered TDEs, which are shown as crosses in pink in Fig. 7. For transients outside of SDSS footprint, we use a looser host galaxy color cut that only requires $g - r > 0.5$ mag using PS1 photometry since the u filter is absent in PS1.

The $u - g$ and $g - r$ colors of the SDSS host galaxies of the nuclear events are shown in Fig. 7. Four CCSNe have been identified with follow up spectroscopy and the colors of their host galaxies are marked in red. As expected, the host galaxies of all four CCSNe have blue colors and are excluded by our empirical host color cut. Transients that are associated with known AGN hosts or classified with follow up spectroscopy are labeled in blue. The host galaxy color cut removes 27 out of 41 (66%) known or newly typed AGNs since a strong blue continuum is usually present in AGN spectra. In this step, we have removed iPTF16bco, which was found to be a changing-look quasar with a continuum flux increase of at least a factor of 10 over $\lesssim 1$ yr (Gezari et al. 2017a).

3.4. Removal of AGNs (Step 4)

There is no physical process restraining TDEs from occurring in an AGN. However, AGNs are much more common (100x) than TDEs in the Universe and most of them exhibit some extent of intrinsic variability that is not of the interest of this study. To optimize the usage of follow up resources, we choose to eliminate transients that are likely due to AGN variability. We first remove known AGNs from the sample of TDE candidates. The candidate sample from step 3 is cross-matched with the 13th edition of quasars and active nuclei catalog (Véron-Cetty & Véron 2010). In addition, we also search SDSS for spectroscopic classification labels in table `SpecObj` and `galSpecInfo`. Nuclear events with host galaxies labelled as `QSO`, and `AGN` are most likely due to intrinsic variability and are removed to narrow down the sample size of candidate TDEs.

Secondly, we remove sources with variability history in PTF and iPTF from the sample since variability is an ubiquitous signature of AGN (e.g. Vanden Berk et al. 2004; Wilhite et al. 2005). We search for detection history in archival PTF and iPTF database from 2009 to 2016 at the coordinates of the nuclear transients. To avoid dubious subtractions, we require at least two detections ($>5\sigma$) on the same night to report the detection as 'real'. A source is removed from the sample if it was detected in at least one of the previous seasons and was not reported as any transient phenomenon other than AGN.

By limiting the search to inactive galaxies only, we have eliminated iPTF16ezh (or PS16dtm) from the sample, which is a unique event that has been reported as a TDE

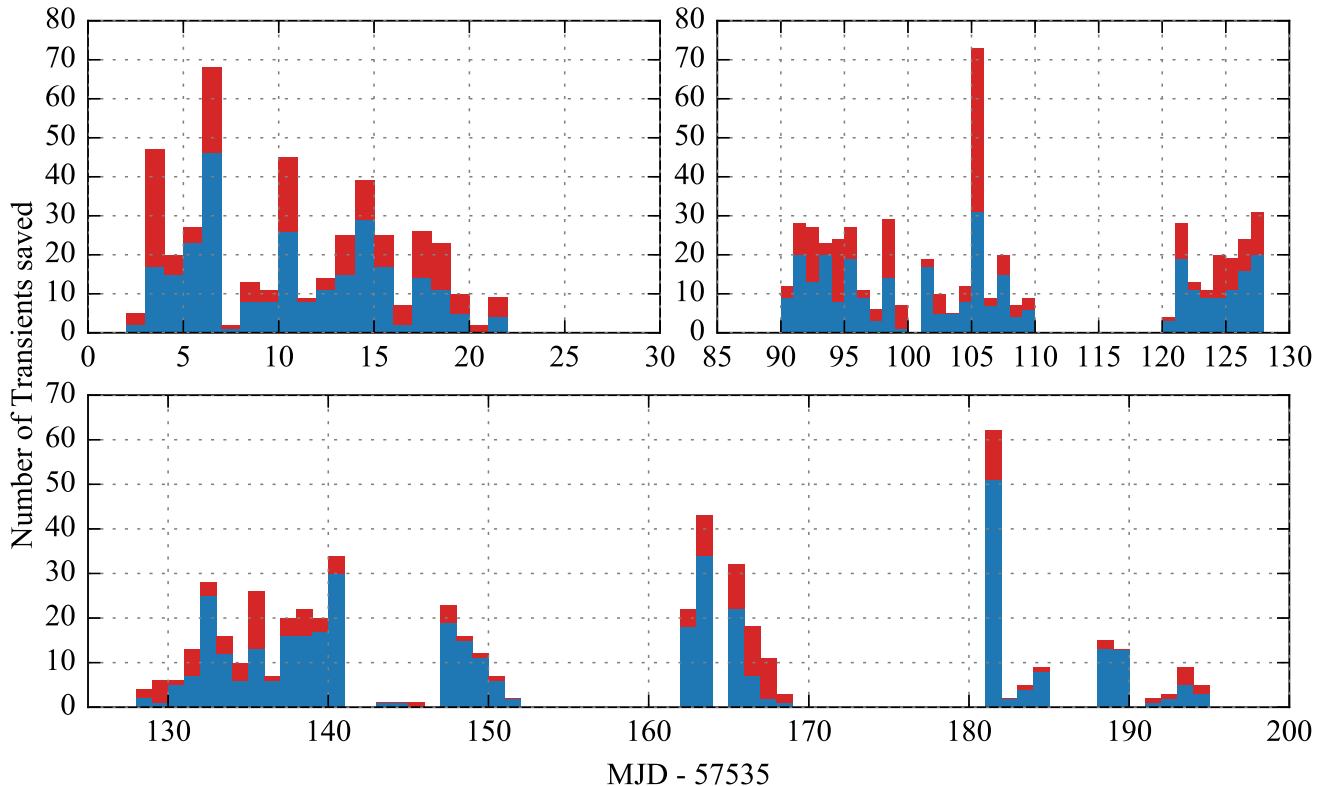


Figure 4. Total number of nuclear (red) on top of non-nuclear (blue) transient events saved during the period of iPTF $g_{\text{PTF}}+R_{\text{PTF}}$ experiment. Nuclear transients account for one-third of all the transients.

in a narrow line Seyfert 1 galaxy at $z = 0.08$ by [Blanchard et al. \(2017\)](#).

3.5. Variability Amplitude Cut (Step 5)

We exclude sources with insignificant variability amplitude by comparing the magnitude of the flare with respect to the PSF magnitude of the host. We define the amplitude of variability (Δm_{var}) as

$$\Delta m_{\text{var}} = -2.5 \log_{10} \left(10^{-\frac{m_{\text{PSF}}}{2.5}} + 10^{-\frac{m_{\text{trans}}}{2.5}} \right) - m_{\text{PSF}}, \quad (3)$$

where m_{PSF} is the PSF magnitude of the host galaxy and m_{trans} is the host-subtracted transient magnitude. We remove nuclear transients with $|\Delta m_{\text{var}}| < 0.5$ mag that can be attributed to small variability from AGNs. By imposing the 0.5 mag variability cut, we are only sensitive to sources with a $>60\%$ flux increase in the nuclear region. This parameter can also be considered as a selection for high contrast against the core of the galaxy.

3.6. Selection of Blue Flares (Step 6)

Since the spectral energy distribution (SED) of optically bright TDEs can be approximated by a blackbody peaking in the UV, these events are intrinsically blue. Therefore, we use $g_{\text{PTF}}-R_{\text{PTF}}$ colors from P48 and P60 to remove redder events that are most likely to be SNe. We query the database to calculate the mean $g_{\text{PTF}}-R_{\text{PTF}}$ color over a timespan of one week from the date of discovery for each source. We correct for Galactic extinction using the [Cardelli et al. \(1989\)](#) extinction curve with $R_C = 3.1$ and $E(B-V)$ values based on

the [Schlafly & Finkbeiner \(2011\)](#) dust map. We do not take the K-correction into account when calculating the color of the flares. Since a TDE spectrum is dominated by a hot blackbody with the optical portion being on the Rayleigh-Jeans tail, the color is not significantly affected by the K-correction. Considering a case where the K-correction would have a greater impact, we assume a blackbody spectrum with $T_{\text{BB}}=2 \times 10^4$ K, which is on the cooler end for TDEs. At $z=0.3$, the $g-R$ color would recover from -0.26 to -0.36 after applying K-correction. The correction on $g-R$ color would be even smaller for TDEs with typical temperature (3×10^4 K) or at a lower redshift.

An important caveat is, however, the host extinction, which is expected to be non-negligible in galaxy nuclei. This value is largely unknown and sometimes may result in the rejection of a transient with a color cut. A steep extinction curve like SMC would redden the $g_{\text{PTF}}-R_{\text{PTF}}$ color by 0.12 mag. Considering these possible reddening mechanisms, we chose a conservative blue flare cut at $g_{\text{PTF}}-R_{\text{PTF}}=0$. We only use g_{PTF} and R_{PTF} pairs that were observed on the same night with the same telescope (P48 or P60) for the color calculation. With the condition $g_{\text{PTF}}-R_{\text{PTF}} < 0$ mag ([Fig. 8](#)), roughly half of the flares were rejected from the sample.

3.7. Brightness Limit for Spectroscopic Follow-up (Step 7)

Finally, we remove sources that were too dim for spectroscopic follow up with 4-meter class telescopes (e.g. DCT) if g_{PTF} or R_{PTF} did not reach <20 mag in 3 days after being saved. The final sample consists of 26 sources.



Figure 5. Flow diagram of the filtering process for TDE candidates. The composition of each intermediate step is listed in Table 1.

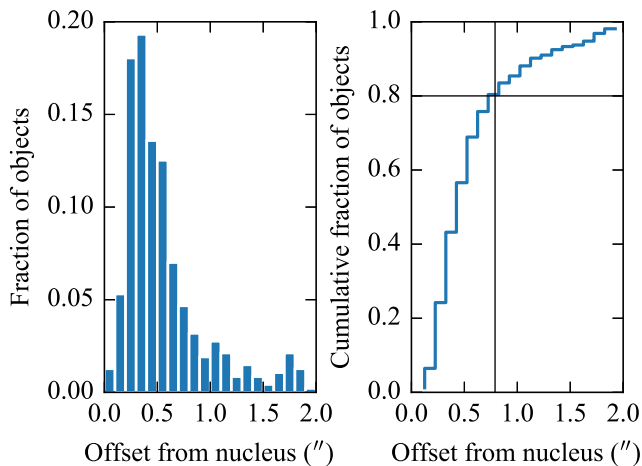


Figure 6. Flare-host separation for transients associated with known AGNs in PTF database (2009–2012). The spatial cut at $d < 0.8''$ includes 80% of the AGNs.

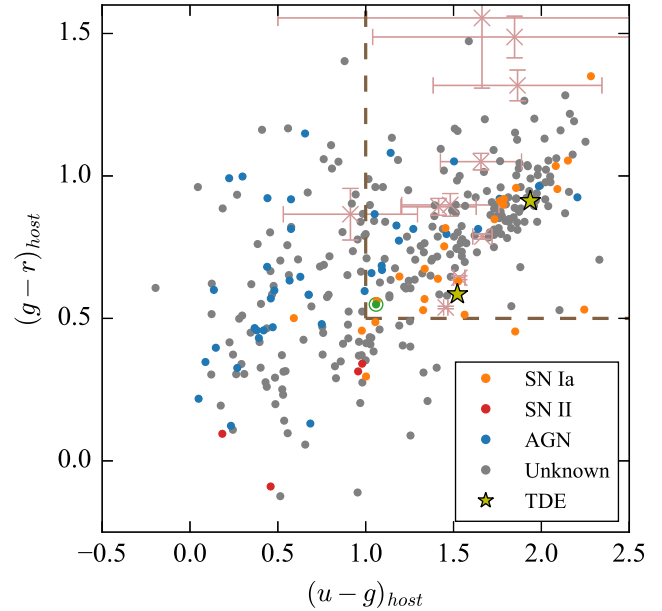


Figure 7. Color-color diagram of the host galaxies of iPTF nuclear transients. An empirical host galaxy color cut for red galaxies is represented by the dashed lines, where sources located in the top right corner satisfy our selection. The pink crosses show the host galaxy colors of previously reported TDEs from four optical surveys: PS1, PTF, SDSS, and ASASSN (see selection of comparison in § 6.2) that are inside SDSS footprint while the two stars mark the two TDEs (iPTF16axa and iPTF16fnl) discovered during this experiment. The only TDE located outside of this dashed box is PS1-10jh. However, a deeper imaging of PS1-10jh does show it satisfying this color selection; it is slightly outside the bounding box because of the high uncertainty in SDSS u photometry. By employing this color cut, we can filter out the CCSNe (red), which are preferentially hosted by blue starforming galaxies as well as a large fraction of AGNs. The green circle marks PS16dtm, which was reported as a TDE in a NLS1 galaxy.

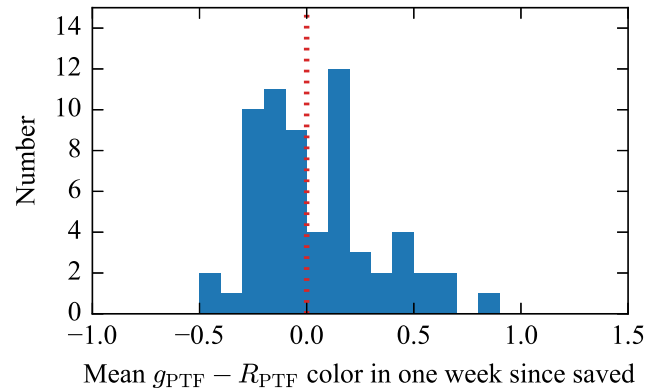


Figure 8. The average $g_{\text{PTF}} - R_{\text{PTF}}$ color of the transients in the first week of discovery. The colors shown here are Galaxy extinction corrected. With the color cut $g_{\text{PTF}} - R_{\text{PTF}} < 0 \text{ mag}$, we removed 30/63 ($\approx 48\%$) of the sources.

4. PHOTOMETRIC AND SPECTROSCOPIC FOLLOW UP

4.1. P48 and P60 photometry

The Palomar 48-inch telescope (P48) is the workhorse of iPTF. During the experiment, the targeted fields were exposed for 60s for each image to reach a depth of ~ 20.5 mag in the g_{PTF} and R_{PTF} bands. The raw images were

detrended and astrometrically and photometrically calibrated at IPAC (Laher et al. 2014).

Follow-up photometric observations with the robotic Palomar 60-inch telescope (P60) was sometimes triggered in *gri* bands to get color and better sampling of the light curve. The P60 raw images were processed by the Fremling Automated Pipeline to be subtracted against the reference images from SDSS (Fremling et al. 2016). We did not obtain any host-subtracted photometry for sources outside of the SDSS footprint with P60.

4.2. *Swift* UVOT and XRT photometry

We triggered Neil Gehrels *Swift* (Gehrels et al. 2004) UVOT (Romig et al. 2005) observations in the bluest *uvw2* (1928 Å) filter from our Cycle 12 Key Project (PI: Gezari) for the classification of iPTF nuclear transients. The exposure time for each *Swift* trigger is 1 ks in order to achieve a limiting magnitude of *uvw2* \sim 23 mag. We used the task `uvotsource` in the HEASoft package to extract the photometry within a 5'' radius aperture in the AB magnitude system.

Simultaneous *Swift* XRT (Burrows et al. 2005) observations were processed by the Swift Data Science Centre pipeline. The pipeline extracts counts from the source in the energy band 0.3 – 10 keV by accounting for dead columns and vignetting.

4.3. SED Machine

The Spectral Energy Distribution Machine (SEDM) is an integral-field-unit (IFU) spectrograph mounted on the P60 telescope (Blagorodnova et al. 2017b). The wide FOV (28''), low resolution ($R \sim 100$) IFU is a powerful tool for classifying transients down to $r \sim 19$ mag. The data obtained by SEDM IFU were automatically processed by the data reduction pipeline, which includes basic image reduction, defining the IFU spatial and wavelength geometry, and spectral extraction. The extracted spectra were flux calibrated with the observations of spectrophotometric standard stars.

4.4. P200 DBSP

We observed with the Double Beam Spectrograph (DBSP) on the 200-inch Hale telescope at Palomar Observatory (P200). A dichroic is used to split the light into a blue and a red component. The observing setup includes a 1'' wide slit and 600g mm⁻¹ grating, giving a dispersion of 1.5 Å pixel⁻¹. The images were reduced with the `pyraf-dbsp` script.

4.5. DCT

Spectroscopic observations were made with the DeVeny spectrograph mounted on the 4.3-meter Discovery Channel Telescope at Lowell observatory. We used a slit width of 1.5'' since the seeing did not get better than 1''. A 300g mm⁻¹ grating was used to achieve a dispersion of 2.2 Å pixel⁻¹. We used standard IRAF routines to reduce the data. The procedures include bias subtraction, flatfielding, aperture extraction, wavelength calibration, and flux calibration.

4.6. Keck LRIS

Spectroscopic observations were made with the Low Resolution Imaging Spectrometer (LRIS; Oke et al. 1994)

on Keck observatory. The observing configuration included a 1'' slit and a 400/3400 grism that gives a FWHM resolution of ~ 7 Å. The data were reduced with the LRIS automated reduction pipeline¹⁶ and flux-calibrated with the standard star BD+28d4211.

5. CLASSIFICATION

The photometric properties of the final sample of 26 candidates are listed in Table 3. Classification spectra were taken for 9 of the candidates. We requested *Swift* UVOT photometry in *uvw2* band for 7 of the high-confidence transients in this final sample that did not have light curves or color evolution resembling a SN Ia or AGN, and did not have a classification spectrum. We describe the classification based on both spectroscopy and photometry in the following sections. Even if a source was not followed-up during the flare, we still obtain spectroscopy of their host galaxies at a later time to measure their redshifts. The host spectra are shown in the Appendix with observing details described in Table 5. The spectroscopic data will be made available via WIS-eREP (Yaron & Gal-Yam 2012).

5.1. Supernovae

5.1.1. Type Ia Supernovae

The similarity in SN Ia light curves has direct application to determining cosmological distances. The SN Ia light curves become even more uniform after accounting for the empirical correlation between the maximum luminosity and the width of the light curve (Phillips 1993), making them the standard candles in the Universe. Unlike CCSNe, SNe Ia do not have a preference for star-forming regions.

In this sample, 5 transients are spectroscopically confirmed SNe Ia classified with the Supernova Identification code (SNID; Blondin & Tonry 2007). For the transients without any follow up spectrum, we inspect the light curves by eye and found 9 transients having burst-like light curves and/or $g_{\text{PTF}} - R_{\text{PTF}}$ color reddening with time that are characteristic of a SN Ia. We label them as ‘‘SN Ia phot’’ in Table 3. A typical SN Ia light curve is characterized by a smooth rise ($\lesssim 20$ days) and decay (~ 0.1 mag per day). Contrary to the lack of color evolution in TDEs, the color of a SN Ia reddens as the ejecta expand with time.

We obtained host spectra for all of these photometric SNe Ia (Fig. A3) in 2017 and measured their redshifts. The peak absolute magnitudes of these photometric SNe Ia are all typical of a SN Ia with m_{peak} around -19 mag. *Swift* observations in *uvw2* for iPTF16fmd and iPTF16gyl were both > 22 mag, which is consistent with the SN Ia classification.

To verify our classification, we perform light curve fitting on all 9 photometric SNe Ia as well as 5 spectroscopically confirmed SNe Ia using the implementation of the SALT2 model in Python package `sncosmo`¹⁷. By fixing the redshift determined from host galaxy spectra, we simultaneously fit light curve data points from both IPAC and NERSC pipelines with the SN Ia time-series model

¹⁶ <http://www.astro.caltech.edu/~dperley/programs/lpipe.html>

¹⁷ <https://github.com/sncosmo/sncosmo>

convolved with filter response in g_{PTF} and R_{PTF} . The key parameters in this model are the date of B -band maximum (t_0), normalization x_0 , light curve stretch x_1 , and the color c . The best-fit light curves of the 8 photometric SN Ia are shown in Fig. 9 while the best-fit parameters of all 14 sources are listed in Table 4. Most of the sources (12/14) have a goodness of fit $\chi^2_\nu < 3.0$. The 2 sources with a slightly larger χ^2_ν include 1 spectroscopic (iPTF16bke) and 1 photometric (iPTF16hcn) SN Ia.

5.1.2. Probable Core-Collapse Supernovae

While confirming the SN Ia classification through light curve fitting, we noticed an outlier, iPTF16bmy, that has a decline too steep to be consistent with a SN Ia light curve. We show the light curve of iPTF16bmy and the best-fit SN Ia light curve ($\chi^2_\nu = 58.8$) in dotted lines in Fig. 10.

We obtained a host spectrum of iPTF16bmy with P200 on Jul 29 2017. The host spectrum of iPTF16bmy (Fig. A4) shows absorption lines dominated by an old stellar population in an elliptical galaxy at $z = 0.129$. The redshift corresponds to a peak magnitude of -18.9 mag in g_{PTF} . The fast rise to peak (< 10 days) would also be unusual for an AGN. The faster rise than decline timescales and the blue color ($g_{\text{PTF}} - R_{\text{PTF}} = -0.14$) near peak resemble the sample of rapidly evolving transients found by Drout et al. (2014), which is likely to have a CCSN origin. All the host galaxies of the rapidly evolving transients have nebular emission lines that are indicative of ongoing star formation. By doing a careful fitting with ppxf (Fig. A4), we do see some weak level of $H\alpha$, [NII], and [OIII] emission. With the information available to us, we classify iPTF16bmy as a “probable” CCSN in Table 3 even though we cannot rule out iPTF16bmy as a subtype of SNIa.

5.2. Variable AGN

We obtained spectra of iPTF16ayd and iPTF16fq during their flaring states and classified them as AGNs. iPTF16ayd was typed as an AGN due to the presence of the broad Balmer emission lines ($\text{FWHM}(H\beta) = 3080 \text{ km s}^{-1}$) that are typical of a Type 1 Seyfert. Although the light curve of iPTF16fq surged by ≈ 2 mag in 60 days, its flaring spectrum does not show broad P-Cygni spectral features like an SN Ia. The *Swift* observation of iPTF16fq showed no X-ray emission though the $uvw2$ magnitude had increased by 1 mag compared to the pre-flare GALEX NUV photometry. While the lack of P-Cygni line and increase in UV flux are both in favor of a TDE origin, we did not notice any $\text{HeII}\lambda 4686$ emission that are often seen in optical TDEs in its flaring spectrum. In addition, we did not detect any change in the optical continuum or the emission line in this source when we made another spectroscopic observation with P200 in 2017. This is at odds with previously detected TDEs, where spectral evolution becomes noticeable on weekly to monthly timescales (e.g. Holoien et al. 2014; Blanchard et al. 2017). The narrow line ratios (Fig. 12) also place this object within the boundary for Seyfert galaxies. The overall spectroscopic properties of iPTF16fq are more consistent with the scenario of a variable AGN.

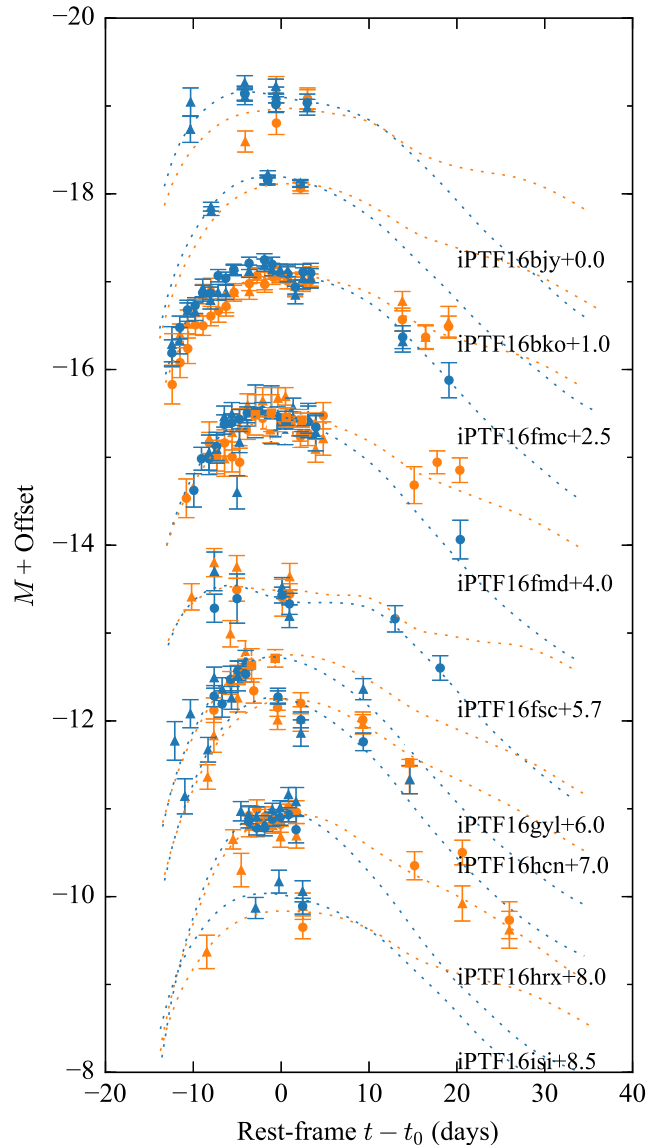


Figure 9. Light curves of the photometric SN Ia in the sample. The blue and orange dotted curves show the best-fit result for g_{PTF} and R_{PTF} band data with the SALT2 model. The circles show the photometry extracted by the IPAC pipeline while the triangles show the photometry extracted by the NERSC pipeline.

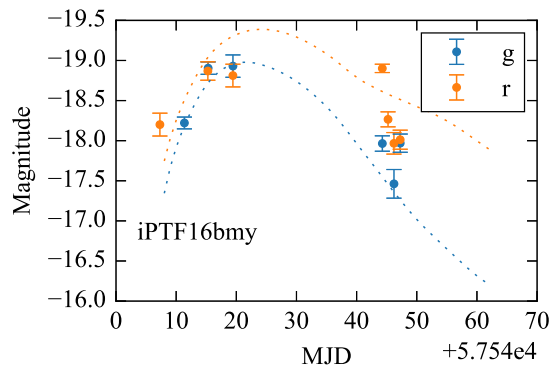


Figure 10. The light curve of iPTF16bmy. The dotted line shows the best-fit SN Ia light curve with $\chi^2_\nu = 58.8$.

We classify 7 other transients in the sample as photometric AGN because their light curves do not have an obvious rising or declining trend. The light curves of all 9 spectroscopic and photometric AGNs in our sample are shown in Fig. 11.

We verify the photometric AGN classification with the host spectra obtained in 2017. Among these 7 photometric AGNs, iPTF16fly, iPTF16fjc, and iPTF16hma have broad Balmer emission lines (Fig. A1). We measure and report the broad H β line widths in Table 5. Among the sources in our sample, iPTF16fly has the highest redshift ($z=0.45$) that the H α is shifted out of the bandpass. We measure the narrow line ratios and plot them on the [OIII]/H β versus [NII]/H α diagnostic diagram (Fig. 12) for AGNs without broad emission lines. Their spectra are shown in Fig. A2. One of these transients, iPTF16fpt, has a pre-flare SDSS spectrum. Because the host spectrum of iPTF16fpt is dominated by the underlying galaxy, we re-measure the line ratios by fitting the SDSS spectrum with `ppxf` (Cappellari 2017), which allows simultaneous fitting of the emission lines and the host galaxy template. We classify iPTF16fhs, iPTF16fpt, iPTF16ijz, and iPTF16fzx as AGNs based on their narrow line ratios as shown in Fig. 12.

All 9 transients that are classified as AGNs have a variability amplitude $|\Delta m_{var}| > 0.7$ mag at peak. Five of them (iPTF16ayd, iPTF16fjc, iPTF16fly, iPTF16fpt, and iPTF16hma) have $|\Delta m_{var}| > 1.0$ mag that satisfies the photometric selection criterion for changing-look quasar (CLQ) candidates in (MacLeod et al. 2016). The flaring spectra for all four objects except iPTF16fpt, which only has a pre-flare SDSS spectrum, exhibit broad Balmer lines. Although we cannot verify whether these four objects have gone through a transition in spectral shape due to the absence of pre-flare spectra, it may be worthwhile to keep an eye on these candidates since some CLQs have shown a reversion to the original spectral class after tens of years (e.g. McElroy et al. 2016).

CLQs are a recently emerged class of objects that exhibit extreme variability in both continuum and emission lines on the timescale of a few years (Shappee et al. 2014; LaMassa et al. 2015; Gezari et al. 2017a). The name refers to the fact that their optical spectra change from a Type 1 to a Type 2 Seyfert or vice versa. Compared to mundane AGNs that only vary by 20% on timescales of months to years (e.g. Hook et al. 1994), CLQs have sparked even more questions on the origin of AGN variability. Currently, it is generally agreed that variable obscuration in the line of sight, lensing of a background quasar, or a tidal disruption event cannot explain every aspect of a CLQ.

This leaves changes in the accretion rate as the favored mechanism for what is causing the CLQs. However, the timescale for viscous perturbations to propagate in a classical thin accretion disk in the UV/optical emitting region ($\approx 100r_g$) is on the order of 10^3 years (Hung et al. 2016), which is much longer than what was observed for CLQs. But this may be resolved if the UV/optical emission of CLQs are irradiated spectrum with variability originating from a smaller radius, where the viscous timescale is effectively reduced.

It has been shown that the difference spectra of quasars could be well fitted by a thin accretion disk spectrum

with changing accretion rates (e.g. Pereyra et al. 2006; Hung et al. 2016), which is consistent with a disk spectrum that follows $f_\nu \propto \nu^{1/3}$ in the optical emitting region. Even in the extreme case of CLQs, it has been reported in some cases that the difference spectra also have power law indices in agreement with a geometrically thin optically thick accretion disk (Gezari et al. 2017b; MacLeod et al. 2016).

The power-law thin disk spectrum corresponds to a $g_{\text{PTF}}-R_{\text{PTF}} \sim -0.1$ mag. The $g_{\text{PTF}}-R_{\text{PTF}}$ colors measured for iPTF16fhs, iPTF16fjc, iPTF16fpt, and iPTF16fzx are consistent with this value, while iPTF16fly, iPTF16fqa, iPTF16hma, and iPTF16ijz are slightly bluer with $g_{\text{PTF}}-R_{\text{PTF}} \sim -0.2$ mag. It is interesting that 3 out of 4 Type 1 Seyferts with broad emission lines, including iPTF16ayd ($g_{\text{PTF}}-R_{\text{PTF}} \approx -0.01$ mag), seem to deviate from the thin disk prediction. As discussed in Hung et al. (2016), the deviation could be caused by the presence of broad emission lines in the bandpass that are also variable. While changes in accretion rate can describe the change in the AGN continuum quite well, variability in the broad emission lines may be driven by different physical mechanisms.

5.3. TDEs

During the rolling $g_{\text{PTF}}+R_{\text{PTF}}$ experiment, iPTF discovered two TDEs, iPTF16axa at $z=0.108$ (Hung et al. 2017) and iPTF16fnl at $z=0.016$ (Blagorodnova et al. 2017a), on UT 2016 May 29 and 2016 August 29, respectively. *Swift* was triggered immediately after the discovery for iPTF16axa. The brightening in the *uvw2* filter along with the strong HeII and H α line in the Keck DEIMOS classification spectrum are both in agreement with the TDE interpretation. iPTF16axa has a persistent blackbody temperature of $\sim 3 \times 10^4$ K throughout the 3-month monitoring period. The light curve of iPTF16axa followed the classic $t^{-5/3}$ power-law decline. No X-ray or radio emission were detected for this source. In Hung et al. (2017), we measured the stellar velocity dispersion with high resolution spectroscopy and derived a black hole mass of $M_{\text{BH}} = 5.0_{-2.9}^{+7.0} \times 10^6 M_\odot$ using the $M-\sigma$ relation in McConnell & Ma (2013). The black hole mass and the overall light curve properties of this source resemble the archetypal TDE PS1-10jh (Gezari et al. 2012).

On the other hand, iPTF16fnl was classified on the same night of discovery by the low resolution SEDm (Blagorodnova et al. 2017b). iPTF16fnl is the nearest (66 Mpc) and also the faintest TDE ever found at optical wavelengths. The light curve of iPTF16fnl declined much more rapidly than the other optically detected TDEs. Whether this decline follows an exponential form or a power-law with a steeper exponent is still debated. iPTF16fnl also has a constant blackbody temperature of $\sim 2 \times 10^4$ K and its host galaxy happens to be an E+A galaxy that features strong H δ absorption.

Both TDEs exhibit strong HeII and H α line in their spectra. The helium-to-hydrogen ratios in these two objects are both higher than what would be expected in a nebular environment with solar abundance of He/H. This suggests that optical depth effects may be important in the line emitting gas in TDEs. For example, high density gas could lead to the suppression of Balmer lines

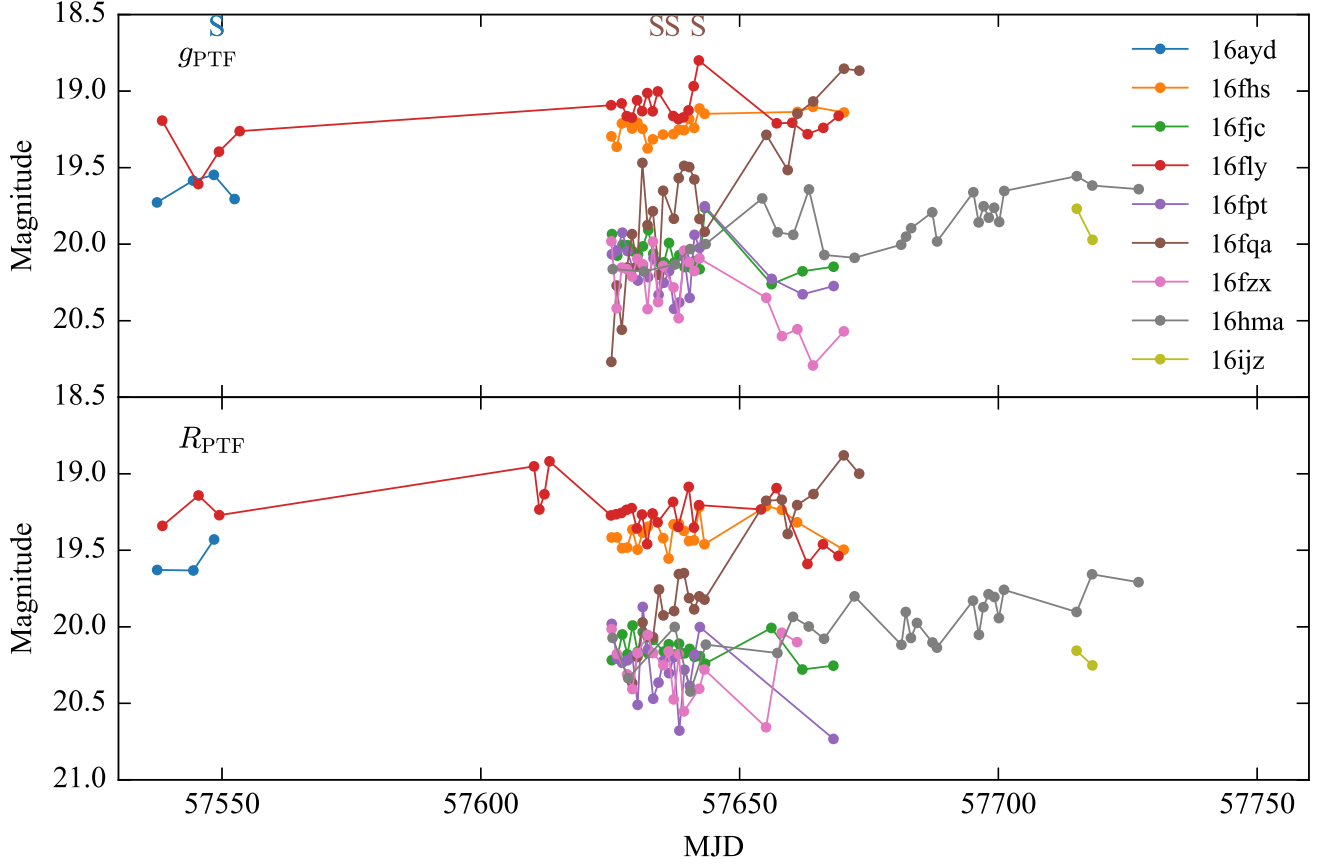


Figure 11. Light curves of the spectroscopically confirmed AGNs and candidate AGNs in our sample. AGN candidates are selected based on their light curves, which lacks obvious rise or fall over the monitoring period. Archival PTF data shows no detection at the positions of the AGN candidates.

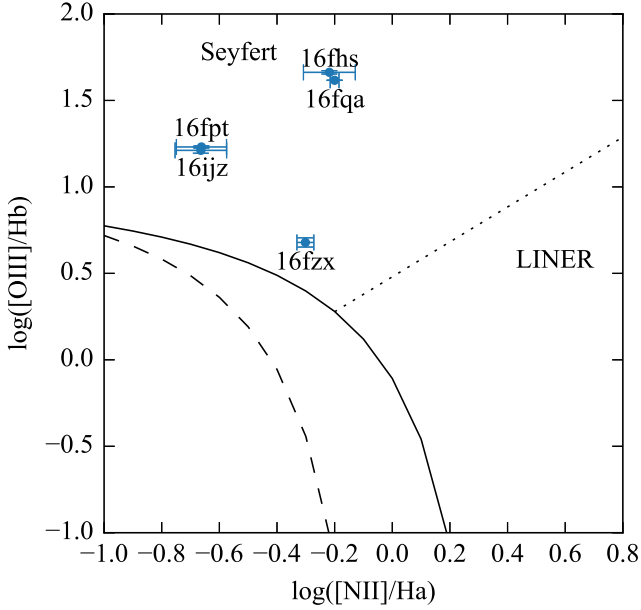


Figure 12. BPT diagram with the solid (Kewley et al. 2001) and dashed (Kauffmann et al. 2003) line separating AGN from star-forming galaxies. The dotted line represents the Seyfert-LINER demarcation (Cid Fernandes et al. 2010). The photometric AGNs that do not have broad Balmer lines are color-coded in blue.

as these transitions become optically thick (Hung et al. 2017; Roth et al. 2016).

5.4. The Swift Sample

We used *Swift* ToO observations in the UV and X-rays under our Cycle 12 program (PI Gezari) to identify TDEs from our high-confidence candidates that do not have light curves resembling a SN Ia or an AGN at the time of discovery. We obtained *Swift* observations for a total of 7 candidates in our sample, 6 of which were scheduled with the time allocated to our Cycle 12 program and 1 (iPTF16fnl) was scheduled through the regular ToO request. We triggered *Swift* on these 6 candidates because we were unable to assign them to any spectroscopic observing runs in the timeframe of 3 days after saving. A separate *Swift* ToO request for a two-months long monitoring campaign was submitted for iPTF16fnl after the rapid classification by SEDm. Details of these *Swift* observations are presented in Table 6. We show the Galactic extinction corrected $g_{\text{PTF}}-R_{\text{PTF}}$ and $uvw2-R_{\text{PTF}}$ color of all the nuclear events in our sample in Fig. 13. The g_{PTF} and R_{PTF} photometry of the flares are chosen to be the nearest to the epoch of the *Swift* observation. We note that although the $g-r$ color of iPTF16gyl had reddened when *Swift* observed it, it had a $g_{\text{PTF}}-R_{\text{PTF}}$ color of -0.3 at the time that we triggered *Swift*. We also plot the mean $g_{\text{PTF}}-R_{\text{PTF}}$ color in the first week of discovery for the AGNs (blue),

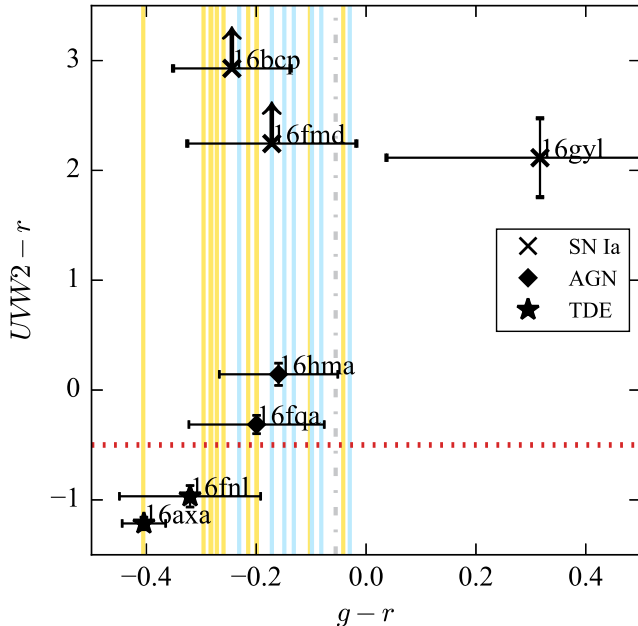


Figure 13. Color-color diagram of the transient events in the sample. The symbols mark sources that were observed by *Swift* and the g_{PTF} and R_{PTF} magnitudes are chosen to be the nearest to the time of the *Swift* observation. The vertical lines show the mean $g_{\text{PTF}} - R_{\text{PTF}}$ color of the sources in the final sample that were not observed by *Swift*. The yellow lines represent sources that are classified as SNe Ia while the cyan lines represent sources that are classified as variable AGNs. iPTF16gyl had a $g_{\text{PTF}} - R_{\text{PTF}}$ color of -0.3 when we triggered *Swift* but has reddened in $g_{\text{PTF}} - R_{\text{PTF}}$ by the time *Swift* observed it.

SNe Ia (yellow), and unclassified sources (grey) in our sample. The two TDEs are well separated from the rest of the non-TDEs in $uvw2 - R_{\text{PTF}} < -0.5$ mag (red dotted line).

While we are able to get rid of the AGNs by adopting a more stringent optical color cut on the flare ($g_{\text{PTF}} - R_{\text{PTF}} < -0.2$ mag), SNe Ia can appear as blue as the TDEs up to one week post peak (e.g. Miller et al. 2017). We therefore conclude that the UV is an important discriminator between TDEs and SNe Ia at early times.

6. DISCUSSION

6.1. Selection on SDSS vs non-SDSS fields

Among the unique fields, 77% (509 out of 660) of the fields also lie within the survey footprint of SDSS DR12. The absence of SDSS data would have direct impact on the selection based on host galaxy properties (§ 3.2, § 3.3) since our selection requires $u - g > 1.0$ and $g - r > 0.5$ and the PS1 survey was conducted without the u band. In our final sample, 19 out of 26 sources were observed by SDSS and have archival SDSS photometry. If we apply the host morphology cut and host galaxy color cut with only $g - r > 0.5$ for PS1 data, our pipeline would end up selecting 35 candidates. All nine additional candidates were rejected in our original selection for being in SDSS footprint but not satisfying $u - g > 1.0$ mag. From this, we estimate the contamination rate to increase by $\sim 35\%$ when only using PS1 data.

6.2. Completeness

In order to determine the completeness of our search, we apply our selection criteria on 10 well-studied TDEs that were discovered by ground-based optical surveys. These 10 TDEs are TDE1 and TDE2 from SDSS (van Velzen et al. 2011), PS1-11af (Chornock et al. 2014), PS1-10jh (Gezari et al. 2012), ASASSN-14ae, ASASSN-14li, ASASSN-15oi (Holoien et al. 2014, 2016b,a), PTF09ge, PTF09axc, and PTF09djl (Arcavi et al. 2014). We do not consider TDEs with $\text{DEC} < -20$ deg (OGLE16aaa (Wyrzykowski et al. 2016), ASASSN-15oi (Holoien et al. 2016a), and ASASSN-15lh (Dong et al. 2016; Leloudas et al. 2016)) here since we require host galaxies information from SDSS or PS1 in our selection.

All ten TDEs pass our selection criteria (see Table 2), with a few caveats described below. All ten TDEs have extended host galaxies and $g - r < 0$ at discovery. The only host galaxy the does not pass our host color cut is that of PS1-10jh, which has $(u - g)_{\text{host}} = 0.91 \pm 0.38$ mag (Fig. 7) according to SDSS. The large error bar in host color is mainly contributed by the faint u band photometry with $u_{\text{host}} = 22.85 \pm 0.37$ mag. In fact, the host color of PS-10jh does satisfy our criteria using a deeper stacked CHFT u band and PS1 g band image (Kumar et al. 2015), which indicates an $(u-g)_{\text{host}} = 2.00 \pm 0.015$ mag.

As mentioned earlier, PS16dtm is rejected by our selection since its pre-outburst archival SDSS spectrum indicates that the host is consistent with a Seyfert galaxy. All ten TDEs have $|\Delta m_{\text{var}}| > 0.5$ mag at peak except TDE1, which has a $|\Delta m_{\text{var}}|$ of 0.3 mag. However, we must note that TDE1 was discovered after peak, and so it likely had a larger amplitude of variability. In sum, our selection criteria are inclusive of all the properties of all optically discovered TDEs hosted by quiescent galaxies.

6.3. Contamination

Our final sample consists of 14 SNe Ia, 9 AGNs, 1 probable core-collapse SN, and 2 TDEs. To investigate if TDEs can be separated from AGN and SN in other parameter space, we use a control sample 26 SNe Ia, 34 AGNs, and 3 TDEs (including PS16dtm) to compare their properties. This control sample consists of spectroscopically classified sources derived from the nuclear transient sample ($d < 0.8''$) in extended host galaxies in this study. We compare the cumulative distribution of different parameter space in Fig. 14 including the absolute peak magnitude in g_{PTF} band, absolute host PSF magnitude in r , apparent host PSF magnitude in r , and Δm_{var} in Fig. 14.

As we pointed out in § 5.4, about 67% (6 out of 9) of AGNs, 43% (6 out of 14) of SNe Ia, and a probable CCSN can be effectively removed in our final sample by employing a more stringent flare color cut of $g_{\text{PTF}} - R_{\text{PTF}} < -0.2$ mag. We notice from panel b and c in Fig. 14 that AGNs have brighter absolute flare magnitudes and absolute host magnitudes compared to TDEs and SNe Ia, which would be two potential ways to remove AGN. Unfortunately, these two parameters require spectroscopy to determine the redshift and it is uncertain if the photometric redshift would be accurate enough for making these cuts. However, we find photometric criteria that can be applied to further reduce the contamination by AGNs and SNe Ia. We verify that $|\Delta m_{\text{var}}| < 0.5$ mag (panel d in Fig. 14) is an effective filter for AGNs. We

Table 2
Applying selection criteria on previously reported TDEs.

Name	ext	red host	Not AGN	No variability	Δm_{var}	$g - r$
SDSS-TDE1	Y	Y	Y	Y	-0.27 ¹	-0.32
SDSS-TDE2	Y	Y	Y	Y	-0.73	-0.31
ASASSN-14ae	Y	Y	Y	Y	-0.54	-0.27
ASASSN-14li	Y	Y	Y	Y	-1.20	-0.41 ³
PS16dtm	Y	Y	N	Y	-2.75	-0.16
PS1-11af	Y	Y	Y	Y	-0.98	-0.30
PS1-10jh	Y	Y ²	Y	Y	-1.21	-0.31
PTF09ge	Y	Y	Y	Y	-1.25	-0.25
PTF09axc	Y	Y	Y	Y	-0.52	-0.04 ³
PTF09djl	Y	Y	Y	Y	-0.97	-0.24 ³

¹ Peak is not resolved in the light curve of TDE1.

² Deeper u band imaging confirms the host galaxy color of PS1-10jh satisfy $u - g > 1$ mag.

³ Since PTF09axc and PTF09djl only have single band light curve, we derive their observed $g - r$ by convolving a redshifted blackbody spectrum with the minimal best-fit temperatures reported in Arcavi et al. (2014), with the g_{PTF} and R_{PTF} response functions, and adding in the Galactic extinction. The same is done for ASASSN-14li since the published g and r photometry include contribution from the host galaxy.

also find that a magnitude cut on the host galaxy of $r_{PSF} < 21.0$ mag removes 25% of the SNe Ia. This is in good agreement with the results of Kumar et al. (2015), who found that a combination of host galaxy apparent magnitude and variability amplitude can be used to discriminate between AGN and SNe, where AGN have brighter host magnitudes and smaller variability amplitudes relative to their host galaxy flux.

In § 3.1 we removed flares that are farther than $0.8''$ away from the centroid of their host galaxies. This offset was calculated by taking the median of all offsets measured from each detection up to the time when the transient was saved. We investigate this condition further by plotting the distributions of the flare-host separation for our control sample with spectroscopically confirmed AGNs (34), SNe Ia (26), and TDEs (3). The histograms of the median separation in the first week of discovery are plotted in Fig. 15.

We noticed that the flare-host separation for AGN peaks toward $0.3''$ while the separation for SN Ia peaks around $0.2''$ and $0.6''$. The TDEs, with a small sample size of 3, all seem to have a nuclear offset of less than $0.2''$. While it is unclear why there seem to be a double-peaked offset for SN Ia, the second peak of SN Ia clearly stands out from the distribution of the nuclear flares. If we place a tighter cut at $d < 0.5''$ we can get rid of 4 out of 14 (29%) of the SNe Ia with the new spatial cut alone.

We compare the composition of our sample selected with the initial selection criteria and the empirical cuts defined in this section in Fig. 17. With the initial selection, we end up with a TDE contamination rate of 13:1 (left panel in Fig. 17). By requiring $g_{PTF} - R_{PTF} < -0.2$ mag to remove AGNs and SNe, we achieve a contamination rate of 6:1 (middle panel in Fig. 17). After applying the spatial cut at $d < 0.5''$ and host galaxy magnitude cut $r_{PSF} < 21.0$ mag, our lowest TDE contamination rate is 4.5:1 (right panel in Fig. 17).

6.4. TDE Rate

The number of TDEs detected by the survey can be expressed as

$$N_{TDE} = \int \frac{d\dot{N}}{dL_g} \times \frac{4\pi}{3} D_{max}^3(L_g) \times \frac{\Delta\Omega}{4\pi} \times \tau dL_g \quad (4)$$

where $d\dot{N}/dL_g$ is the luminosity function of TDEs (the volumetric TDE rate with respect to peak g_{PTF} band luminosity), D_{max} is the maximum distance (redshift) within which a flare can be detected by the flux-limited survey and is a function of the peak magnitude of the flare, $\Delta\Omega$ is the survey area, and τ is the duration of the survey.

We estimate the average timescale of the survey over all the fields by

$$\tau = \sum_{i=1}^N \Delta\tau_{max}/N, \quad (5)$$

where i is the i -th field observed by iPTF, $\Delta\tau_{max}$ is the longest baseline in the $g_{PTF} + R_{PTF}$ survey for the i -th field (right panel of Fig. 2), and N is the total number of unique fields. For fields that are observed before and after the hiatus in summer, we use the longest τ_{max} of these two periods to represent the baseline for the field. By summing over all the unique fields, we find $\tau \sim 44$ days. Since the tidal disruption flares are luminous and long-lasting, the detection is not be sensitive to the week-long observing gaps caused by the full moon. This is true even for fast events like iPTF16fnl, which peaked at $g_{PTF} = 17.07$ mag and faded below 20th mag after 70 days. For iPTF16fnl-like events, which fade by 0.4 mag in the first 7 days post peak, they should remain detectable by iPTF out to $z \sim 0.05$ even in the presence of a week-long gap in the light curve.

We can solve for D_{max} by requiring the apparent magnitude of a source with a given peak luminosity νL_g being above the limiting magnitude $m_g = 20$ mag. We assume a standard blackbody temperature of $T = 3 \times 10^4$ K, which is representative for the optical TDEs, to account for K-correction. The differential flux is expressed as

$$f_\nu = \frac{(1+z)L_\nu(1+z)}{4\pi D_L^2(z)}, \quad (6)$$

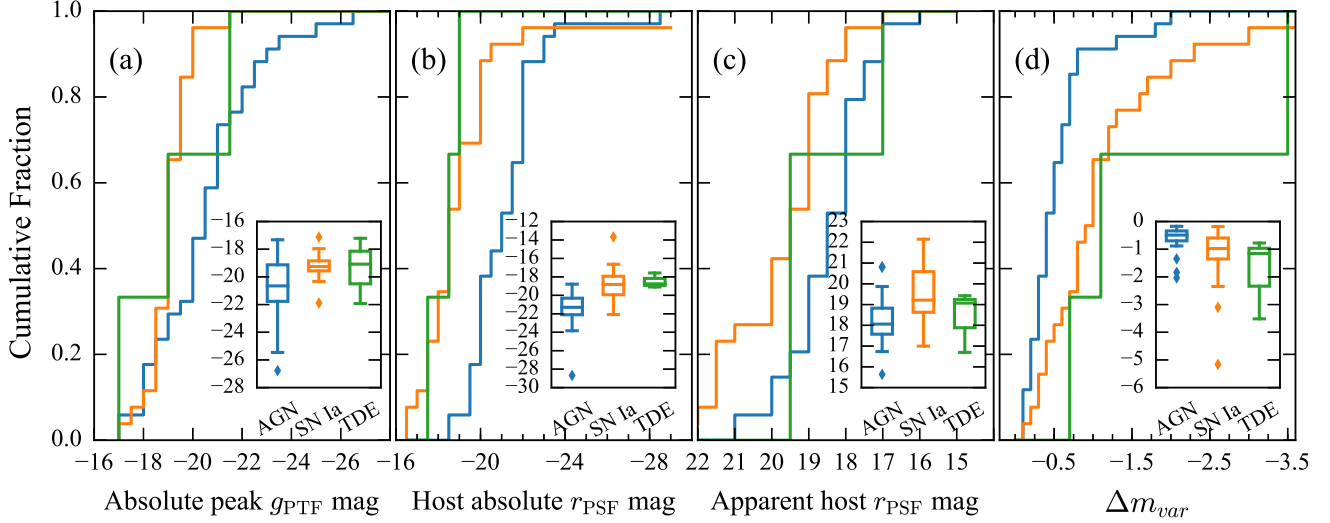


Figure 14. The cumulative distribution of the (a) absolute peak magnitude in g_{PTF} band, (b) absolute host PSF magnitude in r , (c) apparent host PSF magnitude in r , and (d) Δm_{var} for spectroscopically typed nuclear transients with extended hosts. The insets show the distribution of parameters in the form of box plot that marks the interquartile range (IQR) for each object class. Although AGNs appear to be brighter than SNe Ia and TDEs in (a) and (b), it is uncertain if photometric redshift would be accurate enough for making these cuts. A magnitude cut on the host galaxy at apparent $r_{\text{PSF}} < 21.0$ mag may help to remove some of the SNe Ia. Our variability amplitude cut can effectively remove AGNs as shown in (d).

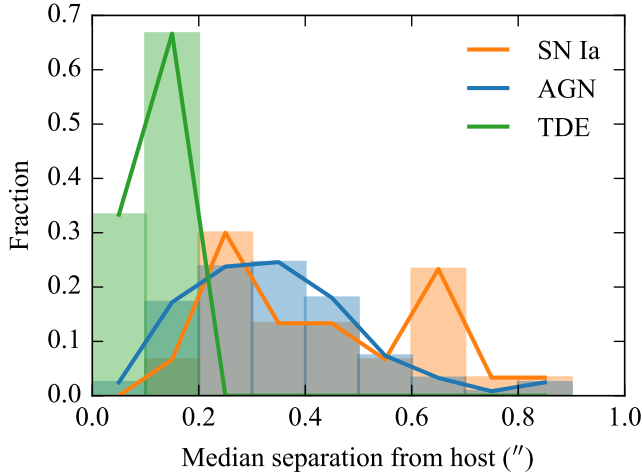


Figure 15. Distribution of the median flare-host separation in the first week of discovery for AGN, SN Ia, and TDEs. Another 41% of the SNe Ia can be removed from our nuclear sample if we employ a spatial cut at $d < 0.5''$.

where f_ν is the observed flux density, $L_{\nu(1+z)}$ is the emitted luminosity density, and D_L is the luminosity distance of the object. We then solve z by converting f_ν back to AB magnitude.

The empirical luminosity function of UV/optical selected TDEs is measured in [van Velzen \(2017\)](#), which can be approximated as a steep power-law where $d\dot{N}/dL_g \propto L_g^{-2.5}$. The luminosity function can then be parameterized at $L_0 = 10^{43}$ erg s^{-1} as

$$\log_{10} \left(\frac{d\dot{N}}{d\log_{10} L_g} \right) = \log_{10}(\dot{N}_0) - 1.5 \log_{10} \left(\frac{L_g}{L_0} \right) \quad (7)$$

We adopt the power-law form of luminosity function

from [van Velzen \(2017\)](#) and substitute in the areal coverage (4792 deg^2) and timescale ($\tau = 44$ days) into [Eq. 4](#). We integrate [Eq. 4](#) from $10^{42} - 10^{43.5}$ erg s^{-1} . The lower integration limit is chosen to include iPTF16fml, which has an observed peak luminosity of $10^{42.3}$ erg s^{-1} in g band. The upper integration limit is chosen since the luminosity bin is not well-sampled beyond $\nu L_g > 10^{43.5}$ erg s^{-1} . The only TDE in this high luminosity bin is ASASSN-15lh, which is thought to be a TDE around a rotating black hole with a mass $> 10^8 M_\odot$ ([Leloudas et al. 2016](#)). We also note that the nature of this event is still debated as it is also interpreted as a highly super-luminous supernova in [Dong et al. \(2016\)](#). Our chosen luminosity range would also include iPTF16axa, which has an observed peak luminosity νL_g of 10^{43} erg s^{-1} . Low luminosity TDEs like iPTF16fml should be harder to see in flux-limited surveys since its detection volume is almost two orders of magnitude smaller than that for events like iPTF16axa. The fact we are seeing both events may suggest a steep TDE luminosity function.

We estimate the pipeline efficiency from [Frohmaier et al. \(2017\)](#), where they investigated the efficiency as a function of the ratio of host galaxy surface brightness to the flux of the flare. Since they estimated the host surface brightness by integrating the counts over a small image size that is close to the size of the PSF, we use the PSF magnitude from PS1 as a proxy for the surface brightness in our calculation. Our variability amplitude (Δm_{var}) cut already places a limit on this ratio. We are only sensitive to flares with $F_{\text{PSF, host}}/F_{\text{PSF, flare}} \lesssim 1.6$ since we required a $\gtrsim 60\%$ increase in the nuclear region in step 5. The median of the $F_{\text{PSF, host}}/F_{\text{PSF, flare}}$ ratio is ~ 0.6 in our sample after applying the Δm_{var} cut. This value corresponds to the $\approx 50\%$ recovery fraction ([Frohmaier et al. 2017, Fig 6](#)).

After applying an efficiency factor of $\epsilon = 0.5$, the 2 TDEs discovered in the iPTF color experiment would

imply a rate of $\dot{N}_0 = 1.1^{+1.8}_{-0.8} \times 10^{-7} \text{ Mpc}^{-3} \text{ yr}^{-1}$. We note that the volumetric rate is a lower limit because our selection is only sensitive to the red galaxies. We account for this bias when calculating the per galaxy rate as detailed below.

The volumetric rate can be converted to a per galaxy rate \dot{n} by dividing the galaxy density that can be estimated from the galaxy luminosity function. We use the luminosity function derived for SDSS in Blanton et al. (2001), which has the form of a Schechter function, to calculate galaxy density (ρ) probed by iPTF. The majority (90%) of the red host galaxies with spectroscopic redshift in our sample have r band magnitudes falling in the range $-22.7 < M_r < -18.9$. Since the more massive black holes cannot produce a tidal disruption flare, we cut off the luminosity at $M_r = -21.5$ mag, which corresponds to a black hole mass of $10^8 M_\odot$ in Tundo et al. (2007).

We also account for the fraction of red galaxies ($u-g > 1.0$ mag and $g-r > 0.5$ mag) in the luminosity range of $-21.5 < M_r < -18.9$ by querying the SDSS database. This fraction is 21% for sources within SDSS footprint (ugr) and 74% for sources with PS1 photometry (gr). Using the source number weighted fraction of 34.8%, we estimate a density ρ of $6.4 \times 10^{-4} \text{ gal Mpc}^{-3}$, implying a TDE rate of $\approx 1.7^{+2.9}_{-1.3} \times 10^{-4} \text{ TDEs gal}^{-1} \text{ yr}^{-1}$. We compare the per galaxy rate derived in this study to the value reported from other X-ray and optical surveys Fig. 16.

Lastly, we note that the TDE rate derived here only applies to TDEs characteristic of the known optically-selected TDE population in inactive galaxies. Our selection method of excluding AGNs and blue galaxy hosts may have the caveat of introducing a systematic error in the TDE rate since the types of TDEs associated with these galaxies are not probed in this work.

6.5. Prospects with ZTF

The camera mounted on P48 has been replaced with a wider FOV camera (47 deg^2) for ZTF, which is almost an order of magnitude upgrade from iPTF. Together with the reduced overhead time, ZTF will be scanning the sky at a rate of $3760 \text{ deg}^2 \text{ hr}^{-1}$. In 2018, 40% of the ZTF operation time will be dedicated to the public survey to monitor $\sim 15000 \text{ deg}^2$ of the sky with a 3-day cadence with near-simultaneous g_{PTF} and R_{PTF} observations.

We define a field as visible at Palomar to have an airmass < 3 for more than 3 hours in one night. The baseline of each field is ~ 8 months. Scaling from this iPTF color experiment to the wider areal coverage and longer baseline for ZTF, we expect to find $\sim 2 \cdot \left(\frac{15000}{4792}\right) \left(\frac{8 \text{ months}}{44 \text{ days}}\right) = 32^{+41}_{-25}$ TDEs in a year.

We estimate ZTF to discover $\left(\frac{15000 \text{ deg}^2 / 3 \text{ day}}{771 \text{ deg}^2}\right) \times 6$ nuclear candidates per night = 39 nuclear candidates per night. The original selection criteria in our nuclear transient pipeline can already get rid of $\sim 95\%$ of the transients, reducing the number of candidates to 2 per night.

We show the classification of the final sample in a pie chart in Fig. 17. By employing the empirical cuts ($g_{\text{PTF}} - R_{\text{PTF}} < -0.2$ mag, $d < 0.5''$, $r_{\text{PSF, host}} < 21.0$ mag) established in this paper, we are able to further reduce the number of contamination from 13:1 down to

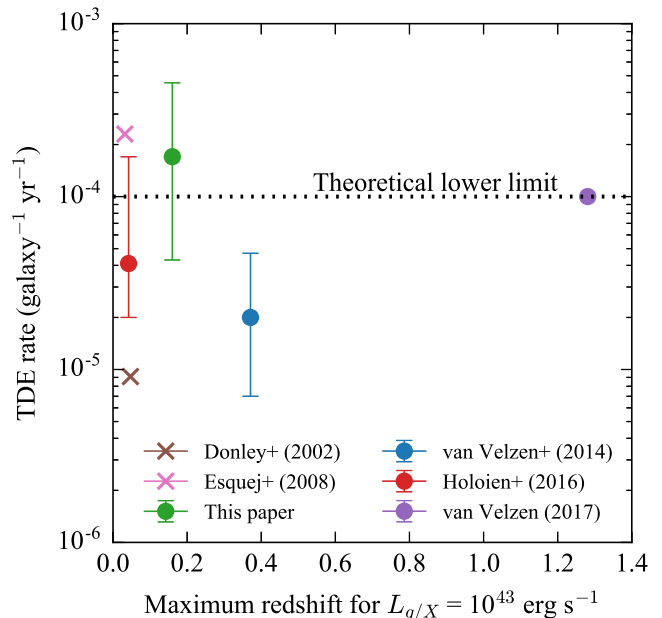


Figure 16. Observational rate of TDEs from X-ray (crosses) and optical (circles) surveys including SDSS+PS1 (van Velzen & Farrar 2014), ASASSN (Holoien et al. 2016b), iPTF (this paper), ROSAT All-Sky Survey (Donley et al. 2002), and XMM-Newton Slew Survey (Esquej et al. 2008). The x-axis shows the maximum redshift for each survey to detect a flare with a peak luminosity of $L_g = 10^{43} \text{ erg s}^{-1}$ for optical surveys or $L_X = 10^{43} \text{ erg s}^{-1}$ in 0.2–2.4keV energy band for X-ray surveys. The dotted horizontal line marks the theoretical lower limit from Wang & Merritt (2004).

4.5:1 (right panel in Fig. 17). The number of nuclear transients satisfying these new criteria will be 0.7 per night for ZTF.

During the operation of ZTF, the low resolution SEDm will be entirely dedicated to spectroscopic follow up of ZTF transients that are brighter than 19 mag in g_{PTF} . In our sample, $\sim 20\%$ of the sources have apparent magnitudes $\lesssim 19.0$ mag near peak, where rapid SEDm classification will be feasible. u band imaging and higher precision astrometry will also help to distinguish between SNe Ia and TDEs, leaving only the highest-confidence TDE candidates. With our selection criteria, the number of candidates that require follow up will be a manageable amount for available spectroscopic resources. With a spectroscopically complete sample of TDEs, we will be able to measure TDE luminosity function and rate that are closely connected to the physical processes leading to the disruption of stars by the central black holes of their host galaxies.

7. ACKNOWLEDGEMENTS

We thank the anonymous referee for helpful comments that improved the manuscript. T.H. thanks Jesper Sollerman for his feedback on the manuscript. S.G. is supported in part by NASA Swift Cycle 12 grant NNX16AN85G and NSF CAREER grant 1454816. These results made use of the Discovery Channel Telescope at Lowell Observatory. Lowell is a private, non-profit institution dedicated to astrophysical research and public appreciation of astronomy and operates the DCT in partnership with Boston University, the University of Maryland, the University of Toledo, Northern Arizona University, and Yale University. The W. M. Keck Ob-

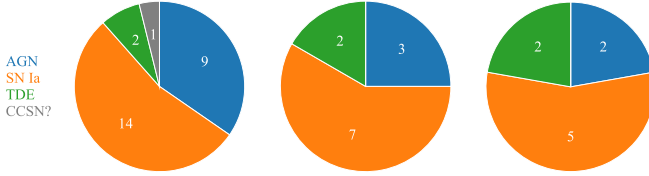


Figure 17. *Left:* Pie charts of the classification in the final sample of 26 sources. *Middle:* After applying the color cut $g_{\text{PTF}} - R_{\text{PTF}} < -0.2$, 6 AGNs and 5 SNe Ia are removed from the sample. *Right:* After applying the spatial cut $d < 0.5''$ and the host galaxy magnitude cut $r_{\text{PSF}} < 21.0$ mag, we are left with 2 TDEs, 5 SNe Ia, and 2 AGNs.

servatory is operated as a scientific partnership among the California Institute of Technology, the University of California, and NASA; the Observatory was made possible by the generous financial support of the W. M. Keck Foundation. This research used resources of the National Energy Research Scientific Computing Center, a DOE Office of Science User Facility supported by the Office of Science of the U.S. Department of Energy under Contract No. DEAC02-05CH11231.

Table 3
Photometric properties of the final sample

Object	redshift	$m_{peak,g}$	$M_{peak,g}$	Δm_{var}	g-r	Classification	Instrument ¹
iPTF16axa ^s	0.108	19.44	-19.08	-1.16	-0.45	TDE	DEIMOS
iPTF16ayd	0.171	19.54	-20.06	-0.54	-0.01	AGN	LRIS
iPTF16bcp ^s	0.14 ^f	19.55	-19.57	-3.10	-0.19	SN Ia	DEIMOS
iPTF16bjy	0.128	19.65	-19.27	-0.52	-0.20	SN Ia phot	
iPTF16bke	0.15 ^f	19.25	-20.01	-0.72	-0.28	SN Ia	LRIS
iPTF16bko	0.085	18.74	-19.22	-1.09	-0.10	SN Ia phot	
iPTF16bmy	0.129	19.94	-18.99	-1.04	-0.14	CCSN?	
iPTF16fhs	0.110	19.08	-19.48	-0.81	-0.12	AGN phot	
iPTF16fjc	0.449	19.56	-22.45	-2.01	-0.11	AGN phot	
iPTF16fjg	0.14 ^f	19.3	-19.83	-0.88	-0.23	SN Ia	SEDM
iPTF16fly	0.349	18.38	-22.99	-1.25	-0.24	AGN phot	
iPTF16fmc	0.139	19.37	-19.75	-1.09	-0.34	SN Ia phot	
iPTF16fmd ^s	0.151	19.75	-20.05	-1.86	-0.17	SN Ia phot	
iPTF16fml ^s	0.016	17.06	-17.21	-0.78	-0.22	TDE	SEDM
iPTF16fpt	0.160	19.52	-19.93	-0.75	-0.12	AGN phot	
iPTF16fqa ^s	0.125	19.1	-19.76	-0.51	-0.21	AGN	SEDM
iPTF16fsc	0.167	19.23	-20.30	-0.64	-0.02	SN Ia phot	
iPTF16fzx	0.125	19.73	-19.13	-0.60	-0.10	AGN phot	
iPTF16glz	0.03 ^f	16.91	-18.7	-5.16	-0.25	SN Ia	SEDM
iPTF16gy1 ^s	0.112	19.82	-18.78	-0.79	-0.08	SN Ia phot	
iPTF16hcn	0.130	19.59	-19.36	-0.99	-0.28	SN Ia phot	
iPTF16hma ^s	0.391	19.48	-22.18	-1.35	-0.20	AGN phot	
iPTF16hrx	0.105	19.29	-19.16	-0.51	-0.28	SN Ia phot	
iPTF16ijw	0.07 ^f	18.15	-19.36	-1.25	-0.20	SN Ia	SEDM
iPTF16ijz	0.151	19.56	-19.73	-0.71	-0.23	AGN phot	
iPTF16isi	0.092	19.45	-18.67	-0.75	-0.30	SN Ia phot	

¹ Objects for which no classification spectrum was taken are left blank.

^s Has *Swift* *uvw2* photometry. Results are summarized in [Table 6](#).

^f Redshift derived from SNID fit to the flaring SN Ia spectra.

Table 4
Best-fit parameters to the SALT2 model

Object	χ^2_ν	redshift	t_0	$x_0 (\times 10^{-4})$	x_1	c
iPTF16bcp	1.03	0.14	57545.6	2.47	1.86	-0.137
iPTF16bke	4.62	0.15	57558.4	2.57	1.87	-0.162
iPTF16fjg	1.54	0.14	57627.4	3.2	0.83	-0.217
iPTF16glz	2.13	0.03	57664.8	36.67	0.98	-0.024
iPTF16ijw	1.73	0.07	57722.1	10.55	2.66	-0.005
iPTF16bjy	1.70	0.128	57550.1	2.0	3.51	-0.14
iPTF16bko	0.49	0.085	57549.1	6.02	1.29	-0.086
iPTF16fmc	0.89	0.139	57639.4	3.15	2.52	-0.108
iPTF16fmd	1.05	0.151	57637.7	2.26	1.18	-0.082
iPTF16fsc	2.07	0.167	57641.4	1.31	6.18	0.021
iPTF16gyl	2.48	0.112	57672.9	1.93	0.37	-0.006
iPTF16hcn	5.18	0.130	57670.6	2.64	-0.17	-0.096
iPTF16hrx	1.62	0.105	57699.5	2.99	-1.04	-0.077
iPTF16isi	1.88	0.092	57725.5	2.8	1.88	-0.185

¹ Best-fit redshift from SALT2 model.

Table 5
Observations of the host galaxies of the photometrically classified sources

Object	z	Date	Telescope	Host class ¹	FWHM _{Hβ} (km s ⁻¹)
iPTF16bjy	0.128	2017-09-15	DCT Deveny	broad line AGN	6199.0
iPTF16bko	0.085	2017-09-15	DCT Deveny	early-type galaxy	...
iPTF16bmy	0.129	2017-07-29	P200 DBSP	early-type galaxy	...
iPTF16fhs	0.110	2017-09-15	DCT Deveny	AGN	...
iPTF16fjc	0.449	2017-09-17	DCT Deveny	broad line AGN	4086.3
iPTF16fly	0.349	2017-09-15	DCT Deveny	broad line AGN	4633.2
iPTF16fmc	0.139	2017-07-29	P200 DBSP	starforming	...
iPTF16fmd	0.151	2017-07-29	P200 DBSP	AGN	...
iPTF16fpt	0.160	2012-06-29	SDSS(host)	AGN	...
iPTF16fzx	0.125	2017-09-15	DCT Deveny	starforming	...
iPTF16gyl	0.112	2017-09-17	DCT Deveny	AGN	...
iPTF16hcn	0.130	2017-09-16	DCT Deveny	AGN	...
iPTF16hma	0.391	2017-07-31	P200 DBSP	broad line AGN	4419.3
iPTF16hrx	0.105	2017-09-15	DCT Deveny	starforming	...
iPTF16ijz	0.151	2017-09-15	DCT Deveny	AGN	...
iPTF16isi	0.092	2017-09-15	DCT Deveny	starforming	...

¹ Host galaxies are classified based on the [OIII]/H β versus [NII]/H α diagnostic diagram.

Table 6
Swift observations of the sample

Object	Phase days	UVW2 ¹ mag	GALEX NUV mag	XRT erg s ⁻¹ cm ⁻²	<i>z</i>	<i>m</i> _{peak,g}	<i>m</i> _{peak,r}	Class	Δm_{var}
iPTF16axa	8.7 ^d	18.77 ± 0.05	...	<1 × 10 ⁻¹⁴	0.108	19.44	19.99	TDE	-1.16
iPTF16bcp	1.7 ^d	>22.60	...	<3.3 × 10 ⁻¹³	0.14	19.55	19.77	SN Ia	-3.10
iPTF16fmd	3.8	>22.02	...	<4.1 × 10 ⁻¹³	0.151	19.75	19.62	SN Ia phot	-1.86
iPTF16fml	0.6	16.32 ± 0.03	19.57	4.6 ^{+3.6} _{-2.0} × 10 ⁻¹⁵	0.016	17.06	17.23	TDE	-0.78
iPTF16fqa	13.8 ^d	19.23 ± 0.06	20.59	<2.7 × 10 ⁻¹³	0.125	18.77	18.87	AGN	-0.51
iPTF16gy1	8.5	22.03 ± 0.31	22.81	<2.7 × 10 ⁻¹³	0.112	19.82	19.35	SN Ia phot	-0.79
iPTF16hma	69.5 ^d	19.78 ± 0.08	...	<5.9 × 10 ⁻¹³	0.391	19.47	19.65	AGN phot	-1.35

¹ Galactic extinction correction applied.

^d If the peak is not clearly sampled in the light curve, we list Δt since iPTF discovery instead.

REFERENCES

- Arcavi, I., Gal-Yam, A., Sullivan, M., et al. 2014, *ApJ*, 793, 38 [1, 6.2, 2]
- Blagorodnova, N., Gezari, S., Hung, T., et al. 2017a, *ApJ*, 844, 46 [1, 5.3]
- Blagorodnova, N., Neill, J. D., Walters, R., et al. 2017b, *ArXiv e-prints*, arXiv:1710.02917 [4.3, 5.3]
- Blanchard, P. K., Nicholl, M., Berger, E., et al. 2017, *ApJ*, 843, 106 [1, 3.4, 5.2]
- Blanton, M. R., Dalcanton, J., Eisenstein, D., et al. 2001, *AJ*, 121, 2358 [6.4]
- Blondin, S., & Tonry, J. L. 2007, *ApJ*, 666, 1024 [5.1.1]
- Bonnerot, C., Rossi, E. M., & Lodato, G. 2017, *MNRAS*, 464, 2816 [1]
- Burrows, D. N., Hill, J. E., Nousek, J. A., et al. 2005, *Space Sci. Rev.*, 120, 165 [4.2]
- Cao, Y., Nugent, P. E., & Kasliwal, M. M. 2016, *PASP*, 128, 114502 [3, 3.1]
- Cappellari, M. 2017, *MNRAS*, 466, 798 [5.2]
- Chornock, R., Berger, E., Gezari, S., et al. 2014, *ApJ*, 780, 44 [6.2]
- Cid Fernandes, R., Stasińska, G., Schlickmann, M. S., et al. 2010, *MNRAS*, 403, 1036 [12]
- Dai, L., McKinney, J. C., & Miller, M. C. 2015, *ApJ*, 812, L39 [1]
- Dilday, B., Smith, M., Bassett, B., et al. 2010, *ApJ*, 713, 1026 [3]
- Dong, S., Shappee, B. J., Prieto, J. L., et al. 2016, *Science*, 351, 257 [6.2, 6.4]
- Donley, J. L., Brandt, W. N., Eracleous, M., & Boller, T. 2002, *AJ*, 124, 1308 [16]
- Drake, A. J., Djorgovski, S. G., Mahabal, A., et al. 2011, *ApJ*, 735, 106 [1]
- Drout, M. R., Chornock, R., Soderberg, A. M., et al. 2014, *ApJ*, 794, 23 [5.1.2]
- Esquej, P., Saxton, R. D., Komossa, S., et al. 2008, *A&A*, 489, 543 [16]
- Fremling, C., Sollerman, J., Taddia, F., et al. 2016, *A&A*, 593, A68 [4.1]
- French, K. D., Arcavi, I., & Zabludoff, A. 2016, *ApJ*, 818, L21 [1]
- Frohmaier, C., Sullivan, M., Nugent, P. E., Goldstein, D. A., & DeRose, J. 2017, *ApJS*, 230, 4 [1, 6.4]
- Gehrels, N., Chincarini, G., Giommi, P., et al. 2004, *ApJ*, 611, 1005 [4.2]
- Gezari, S., Chornock, R., Rest, A., et al. 2012, *Nature*, 485, 217 [5.3, 6.2]
- Gezari, S., Hung, T., Cenko, S. B., et al. 2017a, *ApJ*, 835, 144 [3.3, 5.2]
- . 2017b, *ApJ*, 835, 144 [5.2]
- Graur, O., French, K. D., Zahid, H. J., et al. 2017, *ArXiv e-prints*, arXiv:1707.02986 [1]
- Hao, L., Strauss, M. A., Tremonti, C. A., et al. 2005, *AJ*, 129, 1783 [3]
- Holoien, T. W.-S., Prieto, J. L., Bersier, D., et al. 2014, *MNRAS*, 445, 3263 [5.2, 6.2]
- Holoien, T. W.-S., Kochanek, C. S., Prieto, J. L., et al. 2016a, *ArXiv e-prints*, arXiv:1602.01088 [6.2]
- . 2016b, *MNRAS*, 455, 2918 [6.2, 16]
- Hook, I. M., McMahon, R. G., Boyle, B. J., & Irwin, M. J. 1994, *MNRAS*, 268, 305 [5.2]
- Hung, T., Gezari, S., Jones, D. O., et al. 2016, *ApJ*, 833, 226 [5.2]
- Hung, T., Gezari, S., Blagorodnova, N., et al. 2017, *ApJ*, 842, 29 [1, 5.3]
- Kauffmann, G., Heckman, T. M., Tremonti, C., et al. 2003, *MNRAS*, 346, 1055 [12]
- Kelly, P. L., & Kirshner, R. P. 2012, *ApJ*, 759, 107 [3.3]
- Kewley, L. J., Dopita, M. A., Sutherland, R. S., Heisler, C. A., & Trevena, J. 2001, *ApJ*, 556, 121 [12]
- Kumar, S., Gezari, S., Heinis, S., et al. 2015, *ApJ*, 802, 27 [6.2, 6.3]
- Laher, R. R., Surace, J., Grillmair, C. J., et al. 2014, *PASP*, 126, 674 [4.1]
- LaMassa, S. M., Cales, S., Moran, E. C., et al. 2015, *ApJ*, 800, 144 [5.2]
- Law-Smith, J., Ramirez-Ruiz, E., Ellison, S. L., & Foley, R. J. 2017, *ArXiv e-prints*, arXiv:1707.01559 [1]
- Leloudas, G., Fraser, M., Stone, N. C., et al. 2016, *Nature Astronomy*, 1, 0002 [6.2, 6.4]
- MacLeod, C. L., Ross, N. P., Lawrence, A., et al. 2016, *MNRAS*, 457, 389 [5.2]
- Magorrian, J., & Tremaine, S. 1999, *MNRAS*, 309, 447 [1]
- Masci, F. J., Laher, R. R., Rebbapragada, U. D., et al. 2017, *PASP*, 129, 014002 [3]
- McConnell, N. J., & Ma, C.-P. 2013, *ApJ*, 764, 184 [5.3]
- McElroy, R. E., Husemann, B., Croom, S. M., et al. 2016, *A&A*, 593, L8 [5.2]
- Miller, A. A., Kasliwal, M. M., Cao, Y., et al. 2017, *ApJ*, 848, 59 [2, 5.4]
- Oke, J. B., Cohen, J. G., Carr, M., et al. 1994, in *Proc. SPIE*, Vol. 2198, *Instrumentation in Astronomy VIII*, ed. D. L. Crawford & E. R. Craine, 178–184 [4.6]
- Pereyra, N. A., Vanden Berk, D. E., Turnshek, D. A., et al. 2006, *ApJ*, 642, 87 [5.2]
- Phillips, M. M. 1993, *ApJ*, 413, L105 [5.1.1]
- Phinney, E. S. 1989, in *IAU Symposium*, Vol. 136, *The Center of the Galaxy*, ed. M. Morris, 543 [1]
- Piran, T., Svirski, G., Krolik, J., Cheng, R. M., & Shiokawa, H. 2015, *ApJ*, 806, 164 [1]
- Rees, M. J. 1988, *Nature*, 333, 523 [1]
- Roming, P. W. A., Kennedy, T. E., Mason, K. O., et al. 2005, *Space Sci. Rev.*, 120, 95 [4.2]
- Roth, N., Kasen, D., Guillochon, J., & Ramirez-Ruiz, E. 2016, *ApJ*, 827, 3 [5.3]
- Schlafly, E. F., & Finkbeiner, D. P. 2011, *ApJ*, 737, 103 [3.6]
- Sesar, B., Ivezić, Ž., Lupton, R. H., et al. 2007, *AJ*, 134, 2236 [3]
- Shappee, B. J., Prieto, J. L., Grupe, D., et al. 2014, *ApJ*, 788, 48 [1, 5.2]
- Shiokawa, H., Krolik, J. H., Cheng, R. M., Piran, T., & Noble, S. C. 2015, *ApJ*, 804, 85 [1]
- Stone, N. C., & Metzger, B. D. 2016, *MNRAS*, 455, 859 [1]
- Stone, N. C., & van Velzen, S. 2016, *ApJ*, 825, L14 [1]
- Tundo, E., Bernardi, M., Hyde, J. B., Sheth, R. K., & Pizzella, A. 2007, *ApJ*, 663, 53 [6.4]
- Ulmer, A. 1999, *ApJ*, 514, 180 [1]
- van Velzen, S. 2017, *ArXiv e-prints*, arXiv:1707.03458 [1, 6.4, 6.4]
- van Velzen, S., & Farrar, G. R. 2014, *ApJ*, 792, 53 [16]
- van Velzen, S., Farrar, G. R., Gezari, S., et al. 2011, *ApJ*, 741, 73 [1, 6.2]
- Vanden Berk, D. E., Wilhite, B. C., Kron, R. G., et al. 2004, *ApJ*, 601, 692 [3.4]
- Véron-Cetty, M.-P., & Véron, P. 2010, *A&A*, 518, A10 [3.4]
- Wang, J., & Merritt, D. 2004, *ApJ*, 600, 149 [1, 16]
- Wilhite, B. C., Vanden Berk, D. E., Kron, R. G., et al. 2005, *ApJ*, 633, 638 [3.4]
- Wyrzykowski, L., Zieliński, M., Kostrzewa-Rutkowska, Z., et al. 2016, *ArXiv e-prints*, arXiv:1606.03125 [6.2]
- Yaron, O., & Gal-Yam, A. 2012, *PASP*, 124, 668 [5]

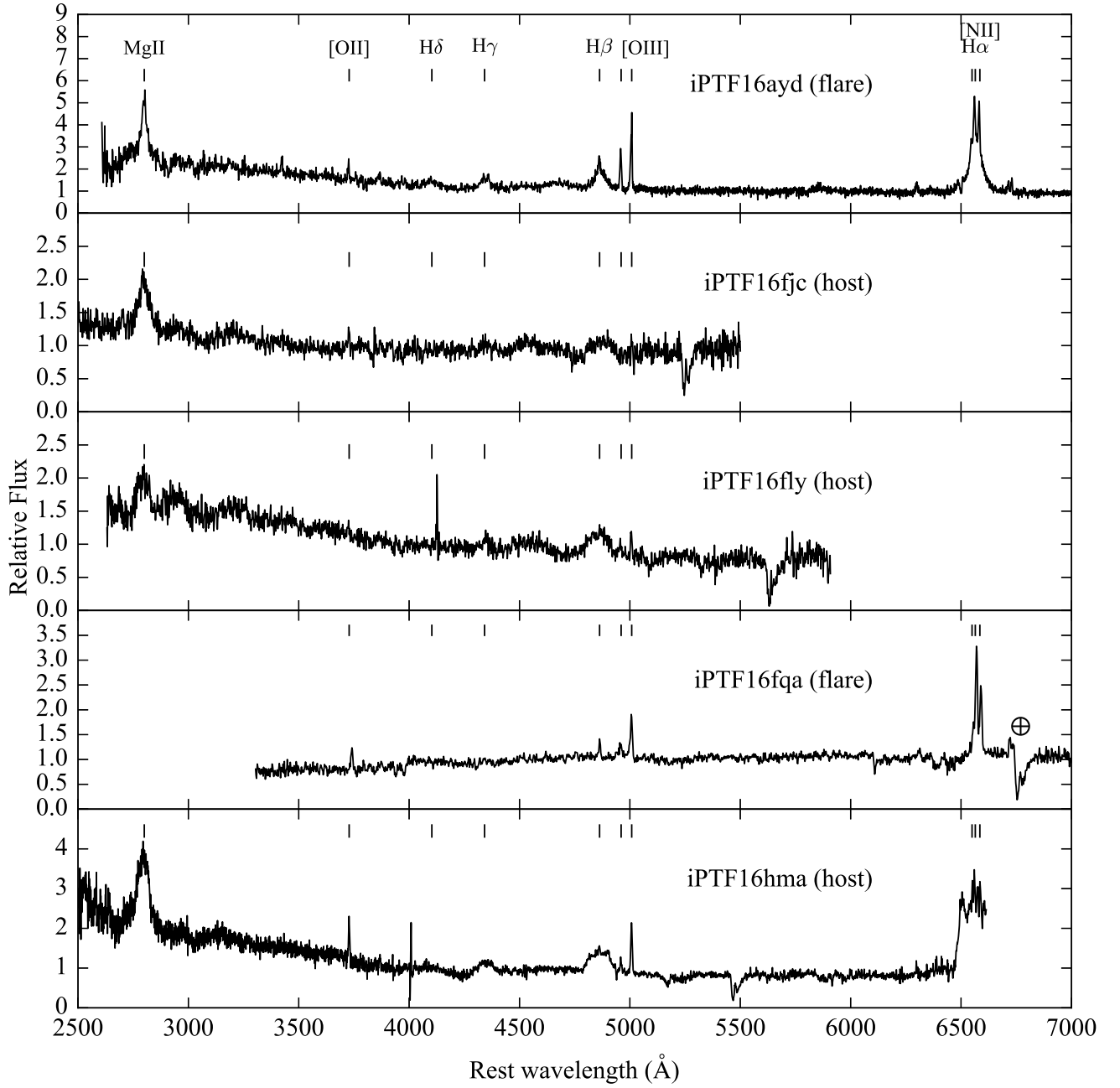


Figure A1. AGNs classified based on the presence of broad emission lines. Strong telluric absorptions are marked with the \oplus symbol.

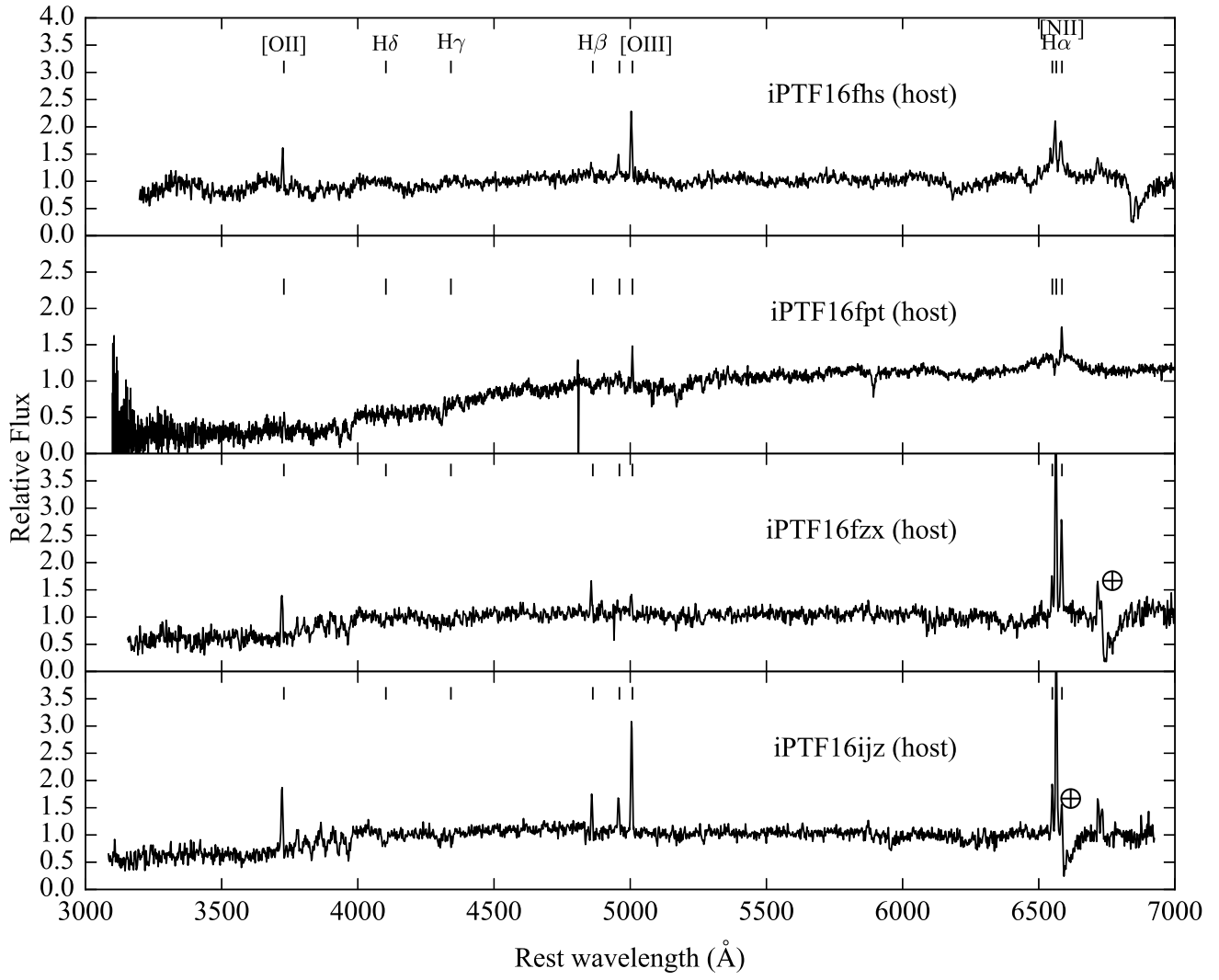


Figure A2. AGNs classified by $[\text{OIII}]/\text{H}\beta$ versus $[\text{NII}]/\text{H}\alpha$ line ratio. Strong telluric absorptions are marked with the \oplus symbol.

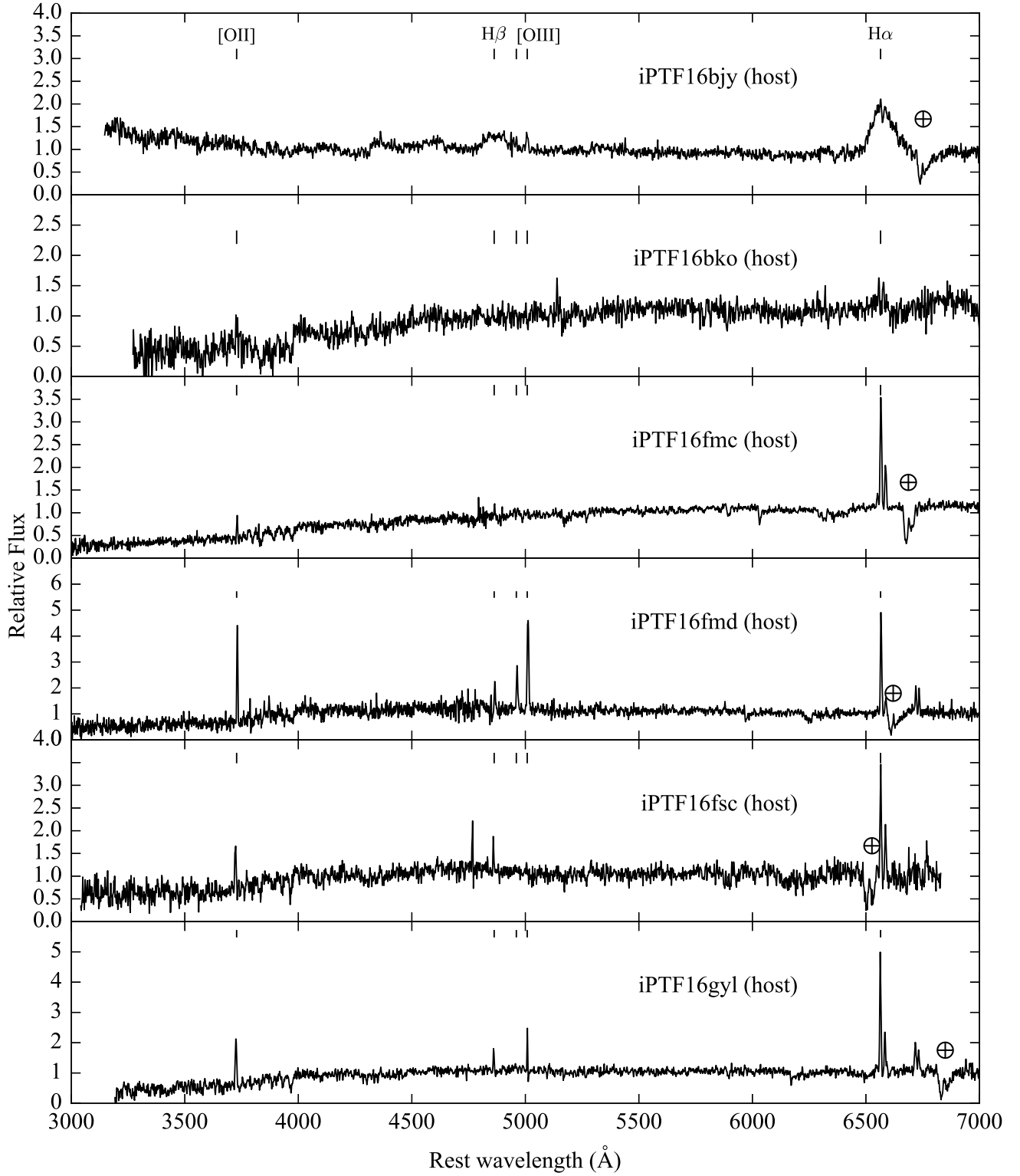


Figure A3. Host galaxies of SNe Ia classified based on the photometry. Strong telluric absorptions are marked with the \oplus symbol.

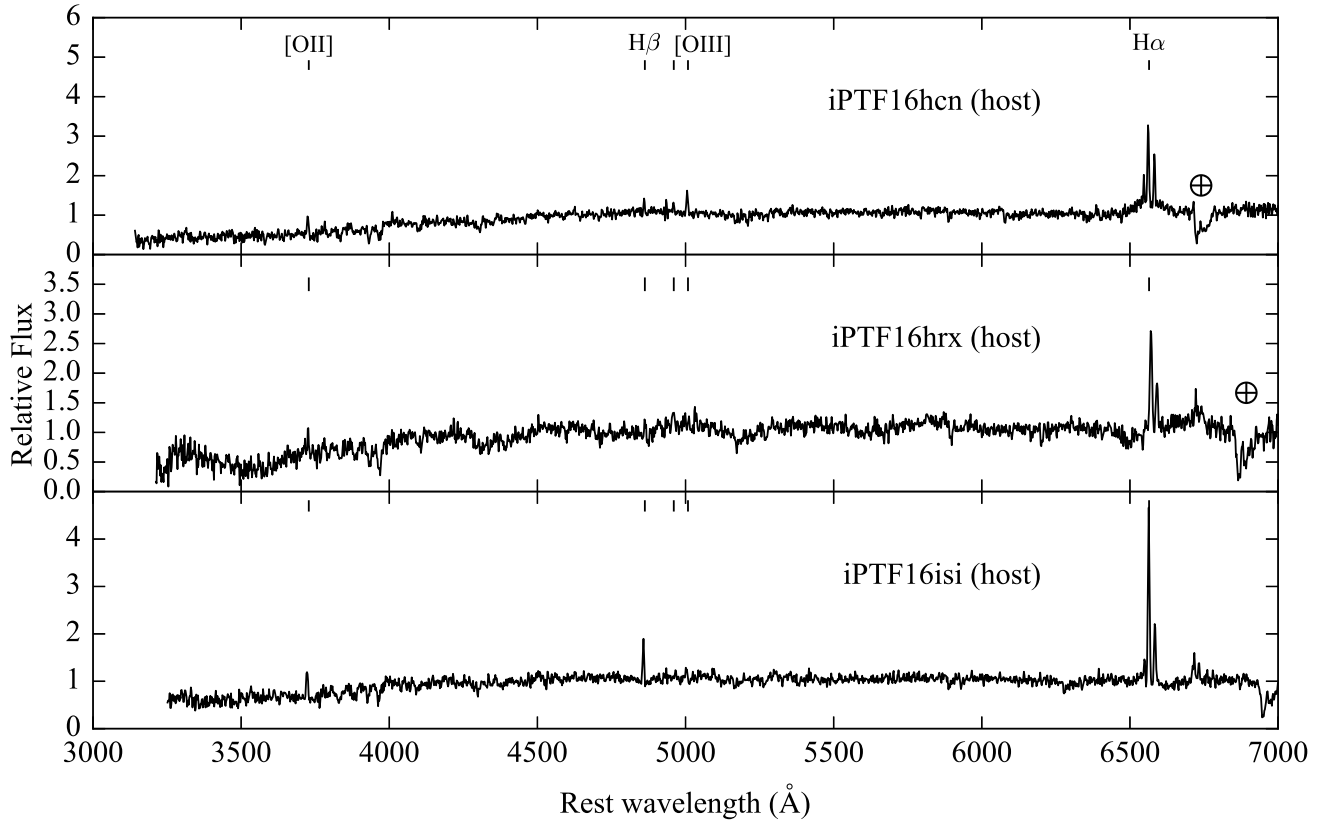


Figure A3. Continued.

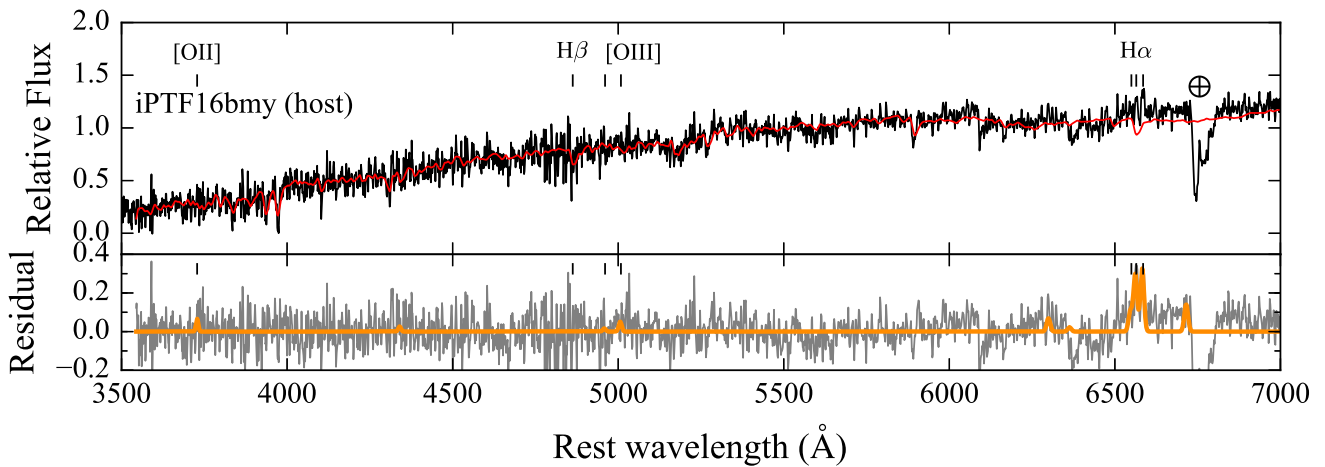


Figure A4. Host spectrum of iPTF16bmy. The black line in the top panel shows the P200 spectrum of the host galaxy of iPTF16bmy while the red line shows the best-fit galaxy spectrum from ppxf. The bottom panel shows the residual of the fit in grey. The emission line profiles that were simultaneously fitted with the stellar templates are colored in orange. Weak $H\alpha$, [NII], and [OIII] lines detected in the host spectrum are suggestive of ongoing starformation.